A Statistical Theory for the "Patchiness" of Open-Ocean Deep Convection: The Effect of Preconditioning

MARK T. DIBATTISTA AND ANDREW J. MAJDA

Courant Institute of Mathematical Sciences, New York University, New York, New York

JOHN MARSHALL

Program in Atmospheres, Oceans and Climate, Department of Earth, Atmospheric and Planetary Sciences, Massachusetts Institute of Technology, Cambridge, Massachusetts

(Manuscript received 1 December 1999, in final form 1 August 2000)

ABSTRACT

Within basins that exhibit open-ocean convection, convectively mixed fluid is often observed in regions of upward-doming isopycnal surfaces, preconditioned by either cyclonic circulation and/or bottom topography. Here, an equilibrium statistical theory for open-ocean convection, developed in the context of two-layer heton models, is adapted to study the outcome of basinwide cooling events over preexisting large-scale ambient flow. A range of prototype ambient flows is studied—including cyclonic and anticyclonic gyres, purely barotropic circulations, and topographically induced flow about a localized seamount and within a broad bowl-like depression. The critical element of these elementary ambient flows is the position of the fluid interface separating the upper and lower layers; it is displaced upward within the cyclonic gyre and the upwelling seamount, downward within the anticyclonic gyre and the bowl-like depression, and is flat for purely barotropic flow. The authors then consider the effect of applying cooling by introducing cold hetons over the preconditioned flow. The most probable postconvection state is found by maximizing the entropy contained in the coarse-grained vorticity field subject to key large-scale constraints. Consistent with observations, the most probable distribution of the cold-temperature anomalies, introduced by the convective overturning that follows a basin-scale surface cold-air outbreak, is indeed concentrated about the peaks of upwelling isopycnals. In contrast, ambient flows with isopycnal surfaces that slope downward fail to confine the cold-temperature anomalies as hetons tend to cluster along the edges and corners of the basin with much weaker displacements.

1. Introduction

a. Background

Open-ocean deep convection, which plays a dominant role in maintaining the thermohaline circulation of the ocean, is observed in a few small basins in the Atlantic Ocean, including the Labrador Sea, the Greenland Sea, and occasionally the Weddell Sea, as well as the Gulf of Lyons in the Mediterranean Sea. In these basins convection is triggered by cold surface winds that sweep across the relatively warm water, removing heat and buoyancy from the ocean surface. The sustained surface cooling often occurs across the basin; however, convective overturning is usually observed in regions of domed isopycnal surfaces induced either by surface wind stresses, as in the Labrador or Mediterranean Sea (Madec et al. 1996), or by topographic steering, as in the Mediterranean Sea (Hogg 1973) or the Weddell Sea (Alverson and Owens 1996). Observations of convection in the Labrador Sea taken during and after deep convection (see Lab Sea Group 1998) reveal a rich horizontal structure of convectively mixed and stratified fluid. Rather than observing a uniformly mixed volume of fluid, there is much "patchiness" on scales of tens to hundreds of kilometers, which is considerably less than the scale of the meteorological forcing or the gyre itself but greater than the ambient deformation scale. At present there is little theoretical understanding of what processes control the "patchiness" of the convectively modified water that remains after the storms that created them have blown themselves out.

The detailed dynamics at work are extraordinarily complicated, involving nonhydrostatic phenomena, mixing, nonlinearities in the equation of state, rotation effects, and intermittency in space and time [for a recent comprehensive survey, see the review by Marshall and Schott (1999)]. But many of these details may not be important in controlling the distribution and properties of the convectively modified waters that remain in the

Corresponding author address: Dr. Andrew J. Majda, Courant Institution of Mathematical Sciences, New York University, 251 Mercer St., New York, NY 10012.
E-mail: jonjon@cims.nyu.edu

© 2002 American Meteorological Society

aftermath of convection. Indeed, we propose to bypass these complications entirely and characterize the preferential congregation of heat and potential vorticity in regions of upwelling isopycnal surfaces, which is the end state of open-ocean convection, as the most probable states of an equilibrium statistical theory. The statistical theory is based on a few bulk conserved quantities related to the strength and duration of the cooling event and is independent of many of the details. The approach may offer a rationale for parameterization of open-ocean convection events without resolving the detailed dynamics.

In particular, we examine the effects of widespread surface cooling over large-scale preconditioned basin flows, including 1) cyclonic or anticyclonic wind-driven gyres and 2) topographically induced flows over seamounts and within basinwide depressions. This study naturally follows work presented in a preceding paper, DiBattista and Majda (2000, hereafter referred to as DM), which examined the distributions of heat and potential vorticity following convective overturning within *quiescent* ambient flow. DiBattista and Majda predicts that, in the absence of a preexisting ambient flow, a statistically homogeneous surface cooling event ultimately yields a cold-temperature anomaly and a potential vorticity anomaly (in only one of the layers) confined to the center of the basin, circumscribed by a stabilizing barotropic rim current. Although the convective forcing is purely baroclinic, the vast majority of the energy—around 90%—in the most probable state is contained in the barotropic portion of the flow.

The predictions of the equilibrium statistical theory in the present work show how these key features are modified by a preexisting flow. In particular, preconditioning that raises isopycnal surfaces, either by wind-driven or topographic means, is extremely effective in localizing convective overturning from a basinwide cold-air outbreak. Cold-temperature and potential vorticity anomalies introduced by convective overturning are confined to the center of the cyclonic gyre and in the region that lies above the upwelling seamount. The energy remains overwhelmingly in the barotropic portion of the flow. In contrast, the thermal and potential vorticity anomalies within the anticyclonic gyre and the downwelling bowl tend to escape to the edges of the domain. This conclusion is in broad agreement with observational and theoretical studies (Madec et al. 1996; Alverson and Owens 1996). Those preconditioned flows that raise the isopycnal surfaces tend to confine the cold temperature anomalies induced by convection near the peak of the isopycnal upwelling, while the preconditioned flows that lower isopycnal surfaces tend to push the cold anomalies near the edges and corners of the basin.

b. Elements of statistical theory applied to open-ocean deep convection

Our equilibrium statistical theory is developed within the context of a two-layer quasigeostrophic fluid model. The ocean basins prone to open-ocean convection typically have a small Rossby deformation radius, which limits the horizontal length scale on which the fluid can convectively overturn (Marshall and Schott 1999). A useful idealization of the localized, geostrophically balanced response to surface cooling, over timescales of a day or so, is a baroclinic pair of counterrotating vortices with cyclonic flow in the upper layers and anticyclonic flow in the lower layers. Within a two-layer fluid this short-term end state of convection is modeled as a heton (Hogg and Stommel 1985), a purely baroclinic alignment of two point vortices of identical strength—positive in the upper layer and negative in the lower layer (Legg and Marshall 1993, 1998; Legg et al. 1996). A basinwide surface cooling event induces a statistical ensemble of localized hetons in the two-layer model. The rate of creation and intensity of the individual hetons can be related to, as described in Legg and Marshall (1993), the history of buoyancy loss at the sea surface.

In DM just three key parameters are used to characterize the convective overturning of a quiescent fluid induced by a basinwide surface cooling event: ΔE, the total energy introduced into the fluid; ΔQ, the strength of an individual heton, which is a function of the peak buoyancy forcing at the surface; and $\Delta\Gamma$, the total circulation anomaly due to the entire ensemble of hetons, which measures the total number of convective towers and depends on the duration and lateral extent of the cooling event [see discussion in section 2b(1) and Fig. 1]. By constructing an equilibrium statistical theory based on just these few parameters and linking the upper- and lower-layer circulations and potential vorticity extrema to the convective process, we tailor a statistical method to find the most probable outcome of the spreading phase of open-ocean convection. Furthermore, there is both rigorous mathematical (DiBattista et al. 1998; Turkington 1999) and computational evidence in more idealized settings (Majda and Holen 1997; Grote and Majda 1997; DiBattista and Majda 2001) for the validity and utility of the predictions of equilibrium statistical theories employing these few constraints.

In the current paper we employ the equilibrium statistical theory to predict the distribution of heat and potential vorticity following cold-air outbreaks over *preconditioned* ambient flow, including cyclonic or anticyclonic gyres and topographically induced flows over localized seamounts or in basinwide bowls. Each of the preconditioned ambient flows are also produced as the most probable states of the statistical theory, defined by their energy, upper- and lower-layer circulations, and potential vorticity extrema. Then, after specifying the surface cooling parameters, ΔE, ΔQ, and $\Delta\Gamma$, we calculate the most probable distribution of heat and potential vorticity following convective overturning in the given ambient flows. The statistical theory predicts that cyclonic gyres and seamounts are extremely effective in localizing convective overturning from a basinwide cooling event. In contrast, anticyclonic gyres, purely

barotropic gyres, and downwelling basin topography fail to localize the cooling, results that are consistent with observations and theoretical studies of open-ocean convection (Madec et al. 1996; Alverson and Owens 1996).

The outline for this paper is as follows. In section 2 we set out the two-layer quasigeostrophic model and discuss the machinery of our equilibrium statistical theory tailored to ocean convection. In section 3 we calculate the elementary ambient flows to be used as preconditioned states for convection. In section 4 the preconditioning effect of wind-driven gyres is investigated; the effect of topographic preconditioning is studied in section 5; and finally, a combination of wind-driven gyres and topographic preconditioning is provided in section 6. Conclusions are drawn in section 7.

2. Formulation and predictions of the statistical theory

We develop the equilibrium statistical theory within the simplest of fluid models for oceanographic flow—a stably stratified, two-layer quasigeostrophic model with nontrivial bottom topography. Here, we relate a few key invariants of ideal two-layer quasigeostrophic flow, which includes the energy, circulation, and potential vorticity extrema in each layer, to the large-scale physical processes that set up the preconditioned ambient flow and force the convective overturning that follows strong surface cooling. The main tool of the statistical theory is a coupled pair of *mean-field equations*, shown in (2.10), whose solutions predict the most probable distributions of heat and potential vorticity throughout the fluid basin. Thus, by linking the key conserved quantities with the critical physical processes that cause convective overturning, we can tailor the mean-field equations to predict the end state of convective overturning within preconditioned ambient flow.

a. Two-layer quasigeostrophic fluid model

We develop the equilibrium statistical theory within the context of a stably stratified, two-layer quasigeostrophic model with nontrivial bottom topography. The fluid evolves in a unit basin with extent $-1/2 < x < 1/2$ and $-1/2 < y < 1/2$. The potential vorticity in the upper and lower layers, q_1 and q_2, and the upper- and lower-layer streamfunctions, ψ_1 and ψ_2, are coupled through the relations (all formulas are nondimensional),

$$q_1 = \Delta\psi_1 - F(\psi_1 - \psi_2)$$
$$q_2 = \Delta\psi_2 + F(\psi_1 - \psi_2) + h_B, \qquad (2.1)$$

where h_B is the nondimensionalized bottom topography and F is the ''rotational Froude number'' (Pedlosky 1979). Here, the symbol $\Delta \equiv \partial^2/\partial x^2 + \partial^2/\partial y^2$ is the Laplacian operator in two dimensions and the nondimensional parameter F is the square of the ratio of length scales, $F = 1/L_\rho^2$, where L_ρ is Rossby deformation radius nondimensionalized by the (unit) basin length scale. Throughout this paper, $L_\rho = 0.05$ ($F = 400$) so that the deformation radius is small with respect to the unit basin length. Thus, for example, if, dimensionally, $L \sim 200$ km, then a nondimensional L_ρ of 0.05 implies a deformation radius of ~10 km, much smaller than the scale of the preconditioned gyre itself. The nondimensional timescale is defined by the rotation period, $1/f$.

The potential vorticities in (2.1) are each materially conserved in the quasigeostrophic model, so that

$$\frac{\partial q_1}{\partial t} + \nabla^\perp\psi_1 \cdot \nabla q_1 = 0$$
$$\frac{\partial q_2}{\partial t} + \nabla^\perp\psi_2 \cdot \nabla q_2 = 0, \qquad (2.2)$$

where the symbol $\nabla^\perp \equiv \mathbf{k} \times \nabla$ is the perpendicular gradient operator. Together with the conditions of no normal flow at the lateral boundaries of the basin,

$$\frac{\partial\psi}{\partial x} = 0, \qquad y = \pm\frac{1}{2},$$
$$\frac{\partial\psi}{\partial y} = 0, \qquad x = \pm\frac{1}{2}, \qquad (2.3)$$

the evolution of the two-layer fluid is completely determined by the initial values of the potential vorticities, q_1 and q_2, in (2.1).

The upper- and lower-layer streamfunctions, ψ_1 and ψ_2, and the upper- and lower-layer potential vorticities, q_1 and q_2, may be split into barotropic and baroclinic components, ψ_B and ψ_T, and q_B and q_T, respectively:

$$\psi_B = \frac{\psi_1 + \psi_2}{2}, \qquad q_B = \frac{q_1 + q_2}{2}$$
$$\psi_T = \frac{\psi_1 - \psi_2}{2}, \qquad q_T = \frac{q_1 - q_2}{2}. \qquad (2.4)$$

Here, the baroclinic streamfunction, ψ_B, measures the portion of the flow that is common to each layer. The baroclinic component of the streamfunction, ψ_T, is proportional to the deformation of the fluid interface between the upper and lower layers in the quasigeostrophic model (Pedlosky 1979):

$$\text{deformation of fluid interface} = -F\psi_T. \qquad (2.5)$$

Since the fluid is of constant density and constant temperature within each layer, with relatively warm fluid atop relatively cold fluid, the position of the fluid interface indicates the relative temperature in a column of fluid. A doming up (upwelling) of the interface contains a greater proportion of colder fluid in the lower layer to warmer fluid in the upper layer and so is relatively cold; similarly, a depression of the interface (downwelling) yields a fluid column that is relatively warm. For this reason we refer to surface plots that show the position of the interface separating the upper and

lower layers of the fluid as the ''thermal field'' and any additional deformation of the interface due to convection as the ''thermal anomaly.''

b. Equilibrium statistical theory

It is easy to show that the quasigeostrophic dynamics given in (2.2) conserves the energy, E,

$$E = -\int q_1\psi_1\, dA - \int (q_2 - h_B)\psi_2\, dA, \quad (2.6)$$

and the circulations in each layer, Γ_1 and Γ_2,

$$\Gamma_1 = \int q_1\, dA \quad (2.7)$$

$$\Gamma_2 = \int (q_2 - h_B)\, dA. \quad (2.8)$$

Furthermore, since quasigeostrophic dynamics conserves the upper- and lower-layer potential vorticities in (2.1), it follows that potential vorticity (PV) extrema,

upper-level extrema:

$$\max(q_1(\mathbf{x})) = Q_{1+}, \qquad \min(q_1(\mathbf{x})) = Q_{1-}.$$

lower-level extrema:

$$\max(q_2(\mathbf{x})) = Q_{2+}, \qquad \min(q_2(\mathbf{x})) = Q_{2-}. \quad (2.9)$$

are also preserved in the evolution of the fluid.

The predictions of the equilibrium statistical theory are expressed as solutions to a coupled pair of elliptic PDEs for the mean-field potential vorticity. These equations arise from maximizing the information (Jaynes 1957) in the coarse-grained potential vorticity field subject to the energy, which resides predominantly in the largest scales, and circulation and PV constraints listed in (2.7) and (2.9), which parameterize the distribution of potential vorticity cloaked in the smallest scales. The solution to the mean-field equations therefore predicts the most probable state of the fluid, given only these few constraints. This procedure is described in detail in DM; here, we simply state the important results, modified to account for bottom topography. The *mean-field equations for two-layer quasigeostrophic flow* are defined as

$$\begin{aligned}\overline{q}_1 &\equiv \Delta\overline{\psi}_1 - F(\overline{\psi}_1 - \overline{\psi}_2) = \overline{Q}_1 + Q_1 L\,[Q_1(\theta\overline{\psi}_1 - \gamma_1)]\\ \overline{q}_2 &\equiv \Delta\overline{\psi}_2 + F(\overline{\psi}_1 - \overline{\psi}_2) + h_B\\ &= \overline{Q}_2 + Q_2 L\,[Q_2(\theta\overline{\psi}_2 - \gamma_2)],\end{aligned} \quad (2.10)$$

where $L[x] = \coth(x) - 1/x$ is the Langevin function and $\overline{Q}_j$ and Q_j are the midpoint and width of the range of potential vorticity in the jth layer,

$$\overline{Q}_j = \frac{Q_{j+} + Q_{j-}}{2} \qquad Q_j = \frac{Q_{j+} - Q_{j-}}{2}, \qquad j = 1, 2. \quad (2.11)$$

The constants, θ, γ_1, and γ_2, are Lagrange multipliers, which ensure that the mean-field potential vorticity in both the upper and lower layers satisfy the constraints listed above, that is, the energy in (2.6) and the circulations in both upper and lower layer in (2.7):

$$\begin{aligned}\theta :\ & -\int \overline{q}_1\overline{\psi}_1\, dA - \int (\overline{q}_2 - h_B)\overline{\psi}_2\, dA = E\\ \gamma_1 :\ & \int \overline{q}_1\, dA = \Gamma_1\\ \gamma_2 :\ & \int (\overline{q}_2 - h_B)\, dA = \Gamma_2,\end{aligned} \quad (2.12)$$

where the mean-field potential vorticities, $\overline{q}_1$ and $\overline{q}_2$, are given in (2.10). In section 2b(1), we show how each of these parameters—the energy, E, the circulations, Γ_1 and Γ_2, and the potential vorticity extrema in the upper layer, Q_{1-} and Q_{1+}, and lower layer, Q_{2-} and Q_{2+}—are expressed in terms of the physical processes that set up the preconditioned ambient gyres and characterize the widespread convective overturning following a strong surface cooling event.

Finally, the most probable states are calculated by an accurate iterative algorithm due to Turkington and Whitaker (1996) that simultaneously determines the mean-field streamfunctions, $\overline{\psi}_1$ and $\overline{\psi}_2$, and the Lagrange multipliers, θ, γ_1, and γ_2, that satisfy the given constraints. See also DiBattista et al. (1998) for more details on the general algorithm.

Parameterization of convective overturning

Within a few days, a strong basinwide surface cooling event will, through deep convective overturning, form many small-scale, geostrophically balanced convective towers scattered throughout the ocean basin (Marshall and Schott 1999). The length scale of these convective towers is controlled by the Rossby radius of deformation, L_ρ, which is very much smaller than the scale of the basin. The induced flow is predominantly baroclinic, with a small-scale cyclone in the upper layers of the ocean lying atop an anticyclone. Within the context of the two-layer quasigeostrophic model, these convective towers have been modeled by purely baroclinic point-vortex hetons (Legg and Marshall 1993, 1998; Legg et al. 1996), which consist of a positive point vortex placed in the upper layer directly atop a matching negative point vortex in the lower layer. The physical content of the ensemble of hetons, each averaged over a deformation radius, is captured within the Langevin statistical theory by just a few parameters: ΔQ, the maximum potential vorticity anomaly introduced into the fluid by convection; $\Delta\Gamma$, a measure of the total potential vorticity introduced into each layer; and ΔE, the energy.

In DM we developed an equilibrium statistical theory for open-ocean convection in initially quiescent flow based on a few conserved quantities; we repeat some

of the arguments here. The parameters ΔQ and $\Delta\Gamma$, which describe the maximum potential vorticity and total circulation in the ocean interior, carry the physical information in the heton model associated with the basinwide cooling event. This can be shown by expressing these parameters explicitly in terms of the surface buoyancy flux, $B_0(\mathbf{x})$, which is directly related to the surface heat loss that controls open-ocean convection. At time and length scales comparable to the earth's rotation, $1/f$, and to the deformation radius, L_ρ, respectively, the towers formed by convective mixing are in approximate thermal wind balance (Legg and Marshall 1993, 1998) so that

$$\Delta Q_{\text{local}} \sim \frac{g'}{f}\frac{\eta}{L_\rho^2}, \tag{2.13}$$

where ΔQ_{local} is the local potential vorticity anomaly over a deformation radius, g' is the reduced gravity in the two-layer model, and η is the average displacement of the fluid interface. In the two-layer model the buoyancy flux, B_0, lost at the surface is balanced by a conversion of upper-layer fluid to lower-layer fluid at the interior interface, the buoyancy per unit volume of which therefore changes by the reduced gravity, g'. Within the timescale, $1/f$, and the length scale, L_ρ, this balance of total surface flux and interior buoyancy loss is approximated by

$$fg'\eta \sim B_0. \tag{2.14}$$

Combining the thermal wind relation in (2.13) and detailed balance of buoyancy in (2.14) yields the strength of the local potential vorticity anomaly, ΔQ_{local}, in terms of a prescribed surface buoyancy forcing, B_0:

$$\Delta Q_{\text{local}} \sim \frac{B_0}{f^2 L_\rho^2}. \tag{2.15}$$

The local potential vorticity ΔQ_{local} can be identified with the heton strength, s, used in Legg and Marshall (1993, 1998) and Legg et al. (1996); in fact, a simple calculation shows that $\Delta Q_{\text{local}} = 2\pi s$.

The parameter ΔQ is a measure of the *strongest* sustained buoyancy forcing averaged over a deformation radius for the duration of the cold-air outbreak. If we imagine that the unit basin is divided into uniform plots each spaced a deformation radius apart, ΔQ_{local} is a local potential vorticity anomaly varying from region to region, depending on the spatial and temporal variability of $B_0(\mathbf{x})$. The parameter ΔQ is the *maximum* value of the local potential vorticity anomalies taken over the entire domain,

$$\Delta Q \sim \max \Delta Q_{\text{local},i}, \tag{2.16}$$

where i is an index for each of the plots spaced a deformation radius apart. In the time that follows a cold-air outbreak, the potential vorticity introduced by surface cooling into each of the localized regions will become thoroughly intermixed, and at sufficiently long times the extrema of the small-scale potential vorticity field will be given by ΔQ at every point in the domain.

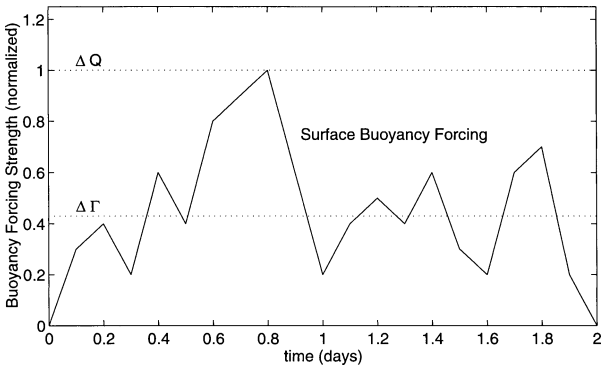

FIG. 1. A schematic representation of a normalized surface buoyancy flux averaged over random plots, each a deformation radius, in the basin over a short time length. The maximum potential vorticity parameter, ΔQ, is proportional to the maximum surface buoyancy flux taken over all plots across the basin, which is indicated by the upper dotted line. The circulation anomaly, $\Delta\Gamma$, is proportional to the average buoyancy flux over all plots across the basin, which is indicated by the lower dotted line.

Finally, the circulation parameter $\Delta\Gamma$ measures the *total* potential vorticity anomaly introduced by the convective forcing so that

$$\Delta\Gamma \sim L_\rho^2 \sum_i \Delta Q_{\text{local},i}, \tag{2.17}$$

where i is the plot index.

The relationship between B_0, ΔQ, and $\Delta\Gamma$ is illustrated in Fig. 1, which shows a hypothetical time series of a normalized surface buoyancy forcing over a short time period at a random location in the basin. The maximum potential vorticity anomaly, ΔQ, is proportional to the maximum level of buoyancy forcing, represented by the upper dotted line. The circulation anomaly, $\Delta\Gamma$, is proportional to the average buoyancy flux across the basin, and is represented by the position of the lower dotted line. Since the parameters ΔQ and $\Delta\Gamma$ parameterize the effects of surface buoyancy flux across the entire basin, ΔQ is proportional to the maximum buoyancy flux taken over all such locations, and $\Delta\Gamma$ is proportional to the total buoyancy removed across the basin.

An important parameter measuring the statistical distribution of convective towers is given by

$$L_T = \sqrt{\frac{\Delta\Gamma}{\Delta Q}}. \tag{2.18}$$

We note that the nondimensional parameter L_T roughly measures the square root of the area that sustains convective forcing divided by the basin area with $0 \le L_T \le 1$. The value of L_T naturally depends on the variability of the surface buoyancy flux, $B_0(x)$. At low values of L_T the buoyancy forcing is intermittent and/or patchy where fewer, stronger hetons are scattered across the

basin. At high values of L_T the buoyancy forcing is more uniform and hetons are spread more evenly across the basin; a uniform cold-air outbreak over the entire basin leads to the maximum condition, $L_T = 1$. The typical value for the patchiness parameter in the paper is $L_T = 0.25$.

3. The basic preconditioned flows with gyres and topography

In DM we calculated the most probable distribution of heat and potential vorticity within a stably stratified, quiescent flow whose surface is cooled strongly enough to induce widespread convective overturning. Observations show, however, that the basins most prone to open-ocean convection are preconditioned by large-scale circulations, either forced by surface winds, induced by bottom topography, or produced by a combination of surface and bottom stresses. In order to separate these contributions and to identify the key elements of the ambient preconditioning, we introduce five prototypical ambient flows: three induced by surface wind forcing—1) a cyclonic gyre, 2) an anticyclonic gyre, and 3) a purely barotropic gyre—and two topographically induced flows—4) one about an upwelling localized seamount and 5) one throughout a basinwide bowl. Convective overturning within the preconditioned wind-forced gyres is treated in section 4; convective overturning within the topographically preconditioned flows is treated in section 5.

As in DM, the modification of heat and potential vorticity distributions through open-ocean convection is calculated by means of the equilibrium statistical theory, described in section 2. Each of the preconditioned flows is a most probable state produced by the statistical theory based on a few conserved quantities consisting of the energy, circulation, and potential vorticity extrema. However, the critical element of the preconditioning is the position of the fluid interface that separates the upper and lower layers in the two-layer model: the interface is pushed upward for cyclonic gyres and upwelling topography, pushed downward for anticyclonic gyres and downwelling topography, and is left undisturbed for purely barotropic flows.

a. Elementary wind-driven gyres

Quiescent ambient conditions over large basins are never observed in nature; the surface winds provide sustained forcing over the upper layers of the ocean, which introduces rotation in the upper reaches of the ocean interior. In the isolated basins that support convective overturning the sense of the large-scale gyres is usually cyclonic with raised isopycnal surfaces that separate the various layers in the ocean (Hogg 1973; Madec et al. 1996). Within the two-layer model, a cyclonic gyre possesses a positive range of potential vorticity in the upper layer, vanishing potential vorticity in the lower layer, and an upwelling of the fluid interface in the basin center. In contrast, an anticyclonic gyre possesses a negative range of potential vorticity in the upper layer, vanishing potential vorticity in the lower layer, and a downwelling of the fluid interface in the basin center. For the purposes of comparison, we also discuss a purely barotropic cyclone, which supports the same strength of flow in both the upper and lower layers, but with no slope introduced to the fluid interface. Finally, we note that the effects of bottom topography are eliminated from the prototype gyres by specifying a flat bottom, $h_B \equiv 0$ in (2.1) so that there is no lower-level potential vorticity associated with the topography.

TABLE 1. Parameters for prototype ambient flows; quiescent condition is zero.

	E	Γ_1	Γ_2	Q_{1-}	Q_{1+}	Q_{2-}	Q_{2+}
Cyclonic gyre	E_G	Γ_G	0	0	Q_G	0	0
Anticyclonic gyre	E_G	$-\Gamma_G$	0	$-Q_G$	0	0	0
Barotropic gyre	E_G	$\Gamma_G/2$	$\Gamma_G/2$	0	Q_G	0	Q_G
Seamount	E_T	0	Γ_T	0	0	0	0
Bowl	E_T	0	Γ_T	0	0	0	0

In these ideal prototypes the elementary gyres in the two-layer fluid are imagined to evolve from a quiescent initial flow forced by surface winds that impart positive or negative potential vorticity into the upper layer. This forcing is sustained over the basin for a time sufficiently long to allow a steady, large-scale rotation to develop in the fluid interior. Physically, the gyres are defined by a minimal set of parameters that capture the interaction of the surface winds with the upper layer of the fluid: the wind imparts energy, large-scale circulation, and a maximum potential vorticity to the upper fluid layer. Potential vorticity is not transmitted to the lower layer, so its potential vorticity remains uniform; however, energy is distributed throughout the fluid and motion is induced in the lower layer by slopes of the fluid interface.

Thus, the cyclonic gyre possesses a positive range of potential vorticity in the upper layer, $[Q_{1-}, Q_{1+}] = [0, Q_G]$, where Q_{1-} and Q_{1+} are the potential vorticity extrema in the upper layer, and a positive circulation, $\Gamma_1 = \Gamma_G$. For the anticyclonic gyre, the range of potential vorticity in the upper layer is negative, $[Q_{1-}, Q_{1+}] = [-Q_G, 0]$, and the circulation in the upper layer, $\Gamma_1 = -\Gamma_G$, is negative as well. For these large-scale gyres the potential vorticity identically vanishes in the lower layer. The parameters that define the cyclonic and anticyclonic gyres are given in Table 1. For the purposes of comparison we also include parameters in this table for a purely barotropic cyclonic flow; here the total circulation is split evenly between the upper and lower layers, that is, $\Gamma_1 = \Gamma_2 = \Gamma_G/2$.

In the top two rows in Fig. 2 we show the velocity fields for the ambient cyclonic and anticyclonic gyres. The two preconditioned flows are defined by identical values of energy, $E_G = 6.3 \times 10^{-5}$, large-scale circu-

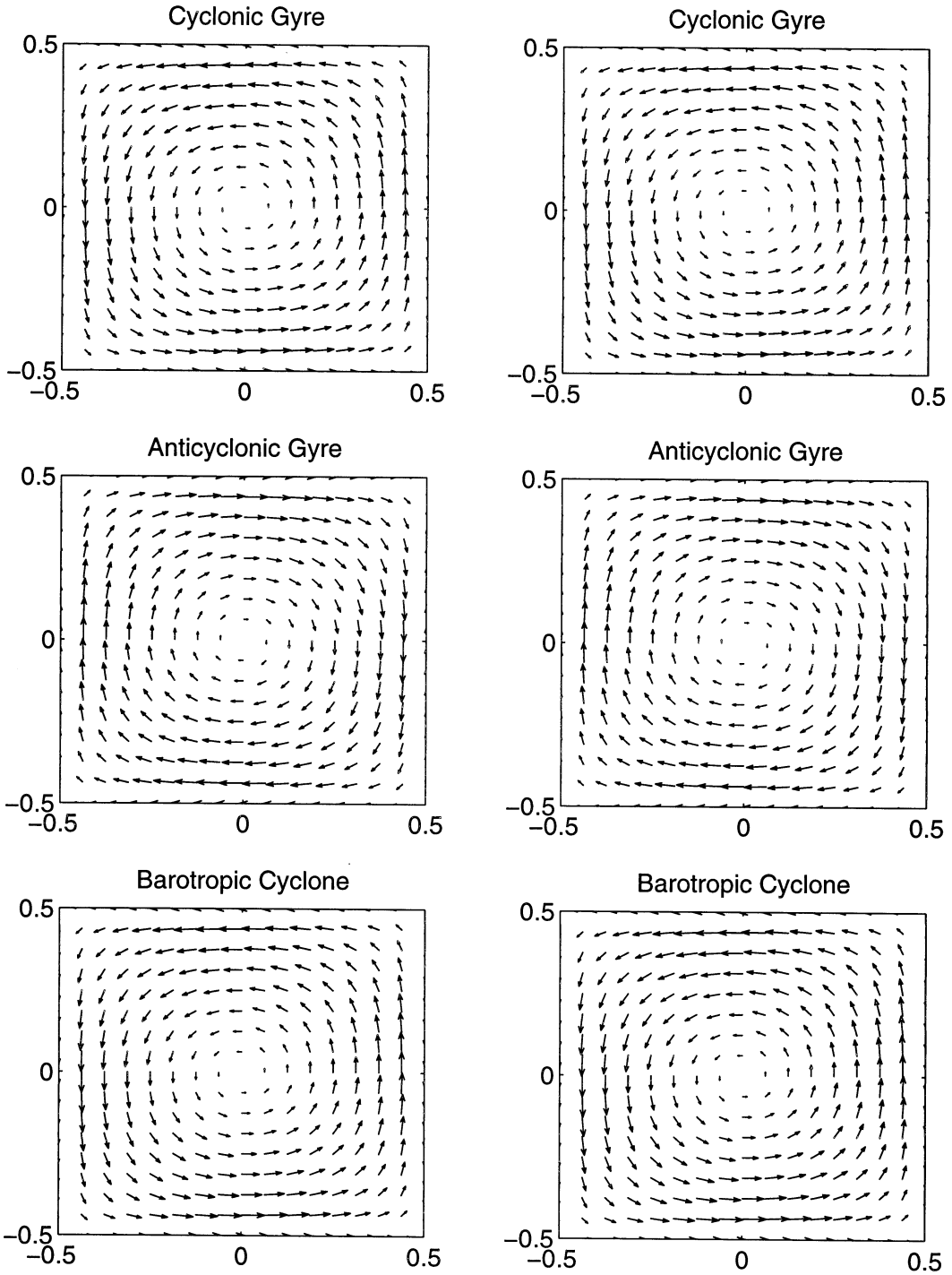

FIG. 2. Upper- and lower-layer velocity fields, located in the left and right columns, respectively, for the prototype wind-driven ambient flows, the cyclonic gyre (top), the anticyclonic gyre (middle), and the barotropic cyclone (bottom). Each of the ambient flow fields is parameterized by $E_G = 6.3 \times 10^{-5}$, $\Gamma_G = 0.07$, and $Q_G = 2.0$.

lation, $\Gamma_G = 0.07$, and potential vorticity extremum, $Q_G = 2.0$, and are symmetric with respect to the sense of rotation. Typical speeds of the large-scale gyres are $u \sim \sqrt{E_G}$. Since $u_{\text{dim}} = Lfu_{\text{non-dim}}$, where L is the scale of the gyre in kilometers and f is the Coriolis parameter, then, dimensionally, $u_{\text{dim}} = 16$ cm s^{-1} taking $L = 200$ km and $f = 10^{-4}$ s^{-1} as typical representative values for the ocean. Given these parameters, each of the gyres is produced as the most probable state of the statistical theory. Here, the energy in the velocity fields is rather

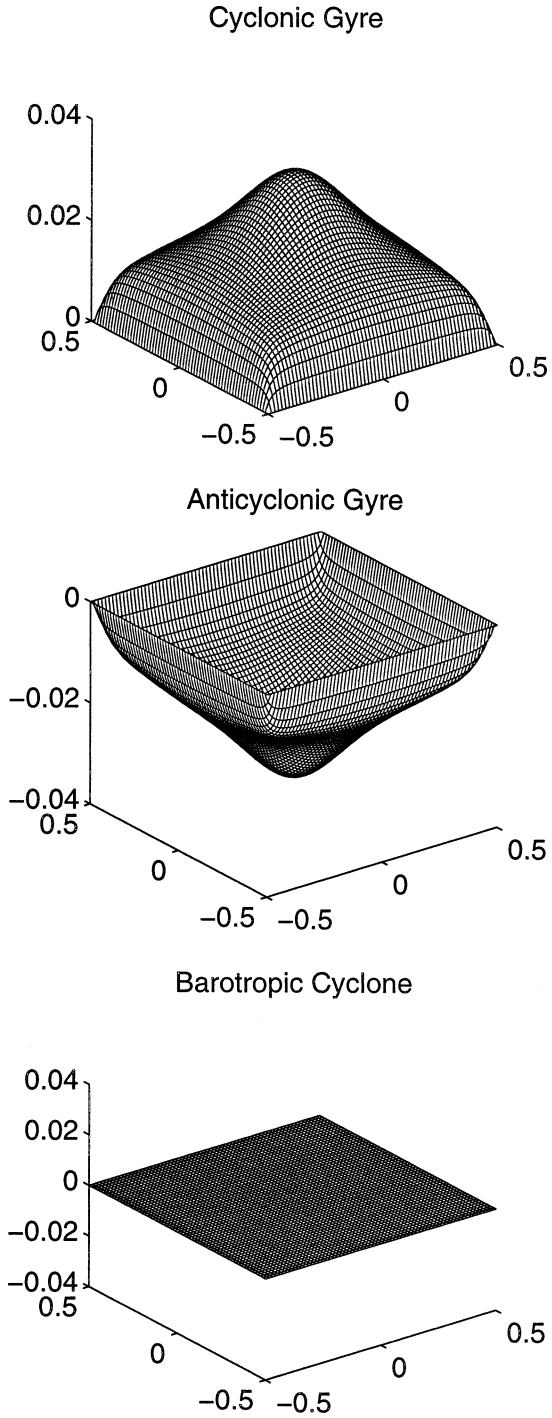

FIG. 3. The preconditioned thermal fields in the ambient cyclonic gyre (top), anticyclonic gyre (middle), and barotropic cyclone (bottom), parameterized as in Fig. 2.

evenly spread throughout the domain. It is easy to manipulate the parameters to produce flows that are concentrated more toward the center of the basin or in jets that run along the boundaries. This is most easily accomplished by altering the circulation, Γ_G: higher levels of circulation leads to strong boundary currents, while lower levels induce tight vortices in the basin center.

In the bottom row in Fig. 2 we show the velocity field for the purely barotropic cyclone with identical values of E_G, Γ_G, and Q_G as the cyclonic and anticyclonic gyre (also, see Table 1). To the eye there is very little difference between the cyclonic gyre in the top row of Fig. 2 and the barotropic cyclone in the bottom row. Moreover, the vast portion of the energy in the cyclonic gyre—approximately 97%—is contained within the barotropic component of the flow, despite the fact that wind-induced potential vorticity does not penetrate the lower layer of the fluid. This phenomenon is a consequence of the small deformation radius, that is, the large value of F. Despite the striking similarity between these two cyclonic large-scale flows, however, we show in sections 4a and 4c that these preconditioned flows behave quite differently under sustained surface cooling that results in convective overturning.

In Fig. 3 we show the preconditioned ambient thermal field, which is directly related to the position of the fluid interface by (2.5), in the cyclonic gyre (top row), the anticyclonic gyre (middle row), and the barotropic cyclone (bottom row). The fluid interface is displaced in different directions in each of the prototype elementary flows: in the basin center the isopycnals dome upward in the cyclonic gyre, dome downward in the anticyclonic gyre, and are flat throughout the basin for barotropic flows. Similarly, the potential vorticity fields in the preconditioned flow, which are not shown, are peaked in the center of the basin—positively for cyclonic flow, negatively for anticyclonic flow—with a width that roughly matches the radius of the doming isopycnals shown in Fig. 3. Since the wind-driven gyres have no lower-layer circulation, the lower-layer potential vorticity fields vanish. We show in section 4 that the position of the fluid interface separating the two layers is the critical feature of preconditioning in the wind-induced gyres.

b. Elementary flows induced by topography

In addition to the large-scale gyres induced by surface wind stresses, the ambient circulation at convection sites can be strongly influenced by the large-scale features of bottom topography. The flow typically follows the contour lines of the bottom surface, revolving anticyclonically above large upwelling seamounts and cyclonically above downwelling depressions (Bretherton and Haidvogel 1976). In this section we introduce two elementary topographic prototypes: 1) a localized Gaussian hill placed in one corner of the basin, which is an idealized model of the topography of the Weddell Sea (Alverson and Owens 1996), and 2) a broad bowl that mimics the gentle slope of the ocean bottom. Within the two-layer quasigeostrophic model, flows induced by bottom topography raise the fluid interface in regions

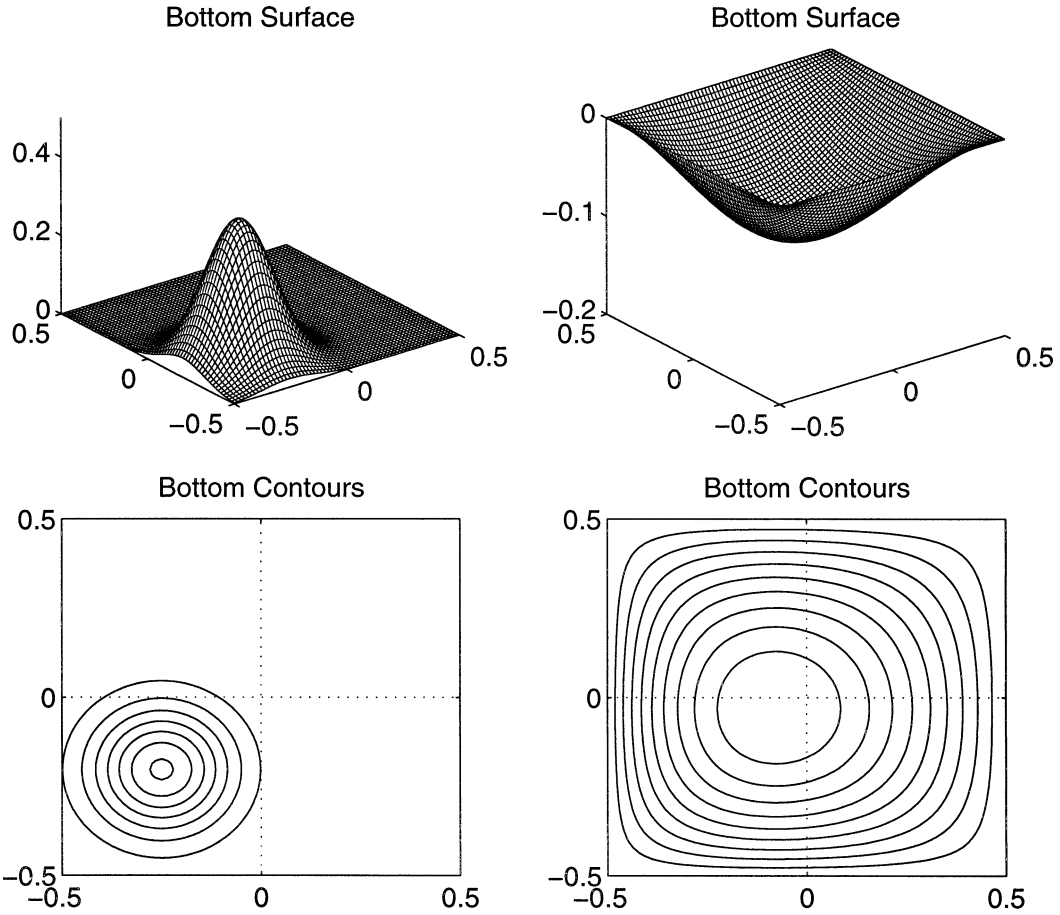

FIG. 4. Two prototype bottom topographies: a localized seamount (left), and a basinwide depression (right). The height of the seamount is given by $H = 0.36$, and the depth of the depression, $H = -0.1$, which yields indentical energies, $E_T = 6.3 \times 10^{-5}$.

of upwelling topography and lower the interface in depressed regions.

We isolate the contribution from bottom topography to the large scale by requiring that the potential vorticity vanish throughout the basin. This eliminates any ambient potential vorticity introduced by the surface wind stress, described in section 3a. If the bottom is flat the resulting flow is naturally quiescent; however, nontrivial bottom topography, that is, $h_B \neq 0$, induces motion in both the upper and lower fluid layers since the streamfunctions, ψ_1 and ψ_2, must satisfy

$$\begin{aligned} \Delta\psi_1 - F(\psi_1 - \psi_2) &= 0 \\ \Delta\psi_2 + F(\psi_1 - \psi_2) &= -h_B, \end{aligned} \tag{3.1}$$

which is a restatement of the PV–streamfunction relations in (2.1) for vanishing potential vorticity.

A localized Gaussian seamount, centered in the lower left corner of the basin, is shown in the left-hand column of Fig. 4. The height of the seamount is given by

$$h_B(x, y) = H \exp\left(\frac{(x_c - x)^2 + (y_c - y)^2}{2w^2}\right), \tag{3.2}$$

where $H = 0.36$ is the maximum height and $(x_c, y_c) = (-0.25, -0.235)$ marks the position of the peak. The breadth of the Gaussian shape is defined by the parameter, $w = 0.125$, which here is 2.5 times as large as the Rossby deformation radius, $L_\rho = 0.05$.

A broad, asymmetric bowl-like depression is shown in the right-hand column of Fig. 4. The depth of the topography is given by

$$h_B(x,y) = H\left[1 - \frac{1 - \frac{x}{x_c}\sqrt{1+x_c^2}}{x - \frac{1}{x_c}\sqrt{1+x_c^2}}\right]\cdot\left[1 - \frac{1 - \frac{y}{y_c}\sqrt{1+y_c^2}}{y - \frac{1}{y_c}\sqrt{1+y_c^2}}\right], \tag{3.3}$$

where $H = -0.1$ is the minimum depth of the bowl. The minimum point of the depression is $(x_c, y_c) = (-0.062, -0.125)$, which is displaced to the lower left-hand corner of the basin. Unlike the seamount defined in (3.2), the horizontal scale of the bowl is the entire length of the unit basin.

In Fig. 5 we show the upper- and lower-layer velocity

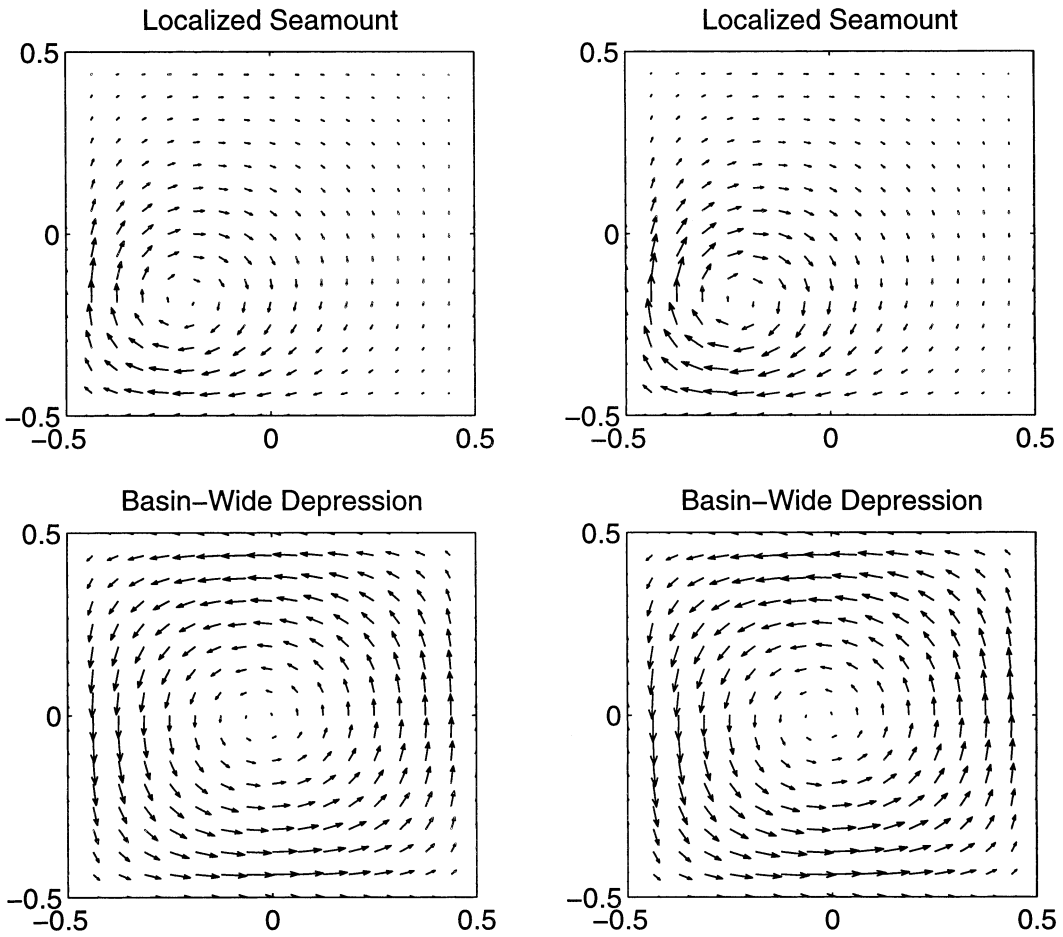

FIG. 5. Upper- and lower-layer velocity fields, located in the left and right columns, respectively, for the prototype ambient flows induced by the localized seamount (top) and the basinwide depression (bottom), parameterized as in Fig. 4.

fields induced by the Gaussian seamount (top row) and asymmetric bowl (bottom row). The height of the seamount and the depth of the bowl are chosen to yield identical values of energy, $E_T = 6.3 \times 10^{-5}$, in the induced large-scale flow. The amount of circulation introduced in the lower layer by each topographic prototype is slightly different, however, with the circulation induced by the seamount being $\Gamma_T = -0.0342$, and the circulation induced by the bowl being $\Gamma_T = 0.0439$. Notice that the flow revolves in a counterclockwise sense above the upwelling seamount and in a clockwise sense above the downwelling bowl. The prototype elementary flows shown in Fig. 5 are produced as the most probable state of the statistical theory, described in section 2b, under the special conditions of vanishing ''vortex inverse temperature'' (DM).

In Fig. 6 we show the preconditioned thermal fields induced by the Gaussian seamount (left-hand column) and the basinwide asymmetric bowl (right-hand column). Here, the displacement of the fluid interface follows the general contours of the topography. The isopycnals above the seamount dome upward at the peak of the hill, and the isopycnals above the bowl are depressed throughout the basin. In section 5 we demonstrate the importance of the upwelling and downwelling in the displacement of the ambient flow when subject to strong surface cooling that results in widespread convective overturning.

c. Convective overturning in preconditioned ambient flows

It is now a simple matter to parameterize convective overturning within the preconditioned ambient flows described in sections 3a and 3b. As described in section 2b(1), the physical content of large-scale surface cooling is captured in three parameters: ΔQ, the maximum potential vorticity anomaly introduced into the fluid by convection; $\Delta\Gamma$, proportional to the total number of hetons introduced into each layer; and ΔE, the energy.

Each of the preconditioned ambient flows is described by an energy, and upper- and lower-layer circulations

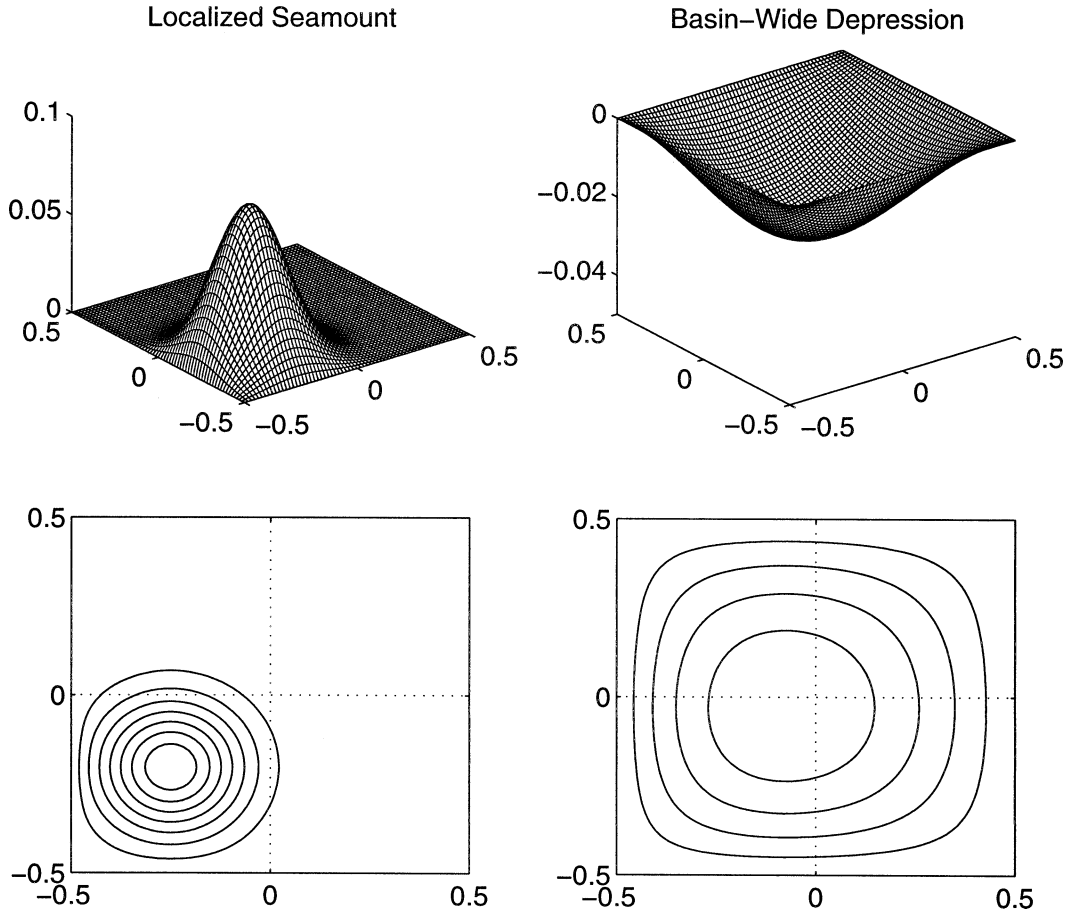

FIG. 6. The preconditioned thermal fields in the flow induced by the localized seamount (left) and the basinwide depression (right), parameterized as in Fig. 4.

and potential vorticity extrema. In Table 2 we provide the total values for these key invariants for convective overturning in ambient quiescent flow (top row) and within wind-driven gyres and topographically steered ambient flows. The vortical invariants associated with convective forcing, which includes the potential vorticity and circulation anomalies, introduce positive quantities in the upper layer and negative quantities in the lower layer. This is shown directly in the top row of Table 2 for convective overturning in quiescent ambient flow in which the upper-layer circulation and potential vorticity extrema are $\Delta\Gamma$ and ΔQ, respectively, and the lower-layer circulation and potential vorticity extrema are $-\Delta\Gamma$ and $-\Delta Q$. Comparing the parameterization of surface cooling over preconditioned flows in Table 2 with the ambient conditions provided in Table 1 shows a similar kind of addition of circulation and potential vorticity maximum in the upper layer and a subtraction of circulation and potential vorticity minimum in the lower layer. For simplicity, the energy associated with convective overturning is also added to the energy contained in the ambient flows.

TABLE 2. Parameters for convective overturning in the prototype ambient flows.

	Ambient flow						
	E	Γ_1	Γ_2	Q_{1-}	Q_{1+}	Q_{2-}	Q_{2+}
	Quiescent						
	ΔE	$\Delta\Gamma$	$-\Delta\Gamma$	0	ΔQ	$-\Delta Q$	0
Cyclonic gyre	$E_G + \Delta E$	$\Gamma_G + \Delta\Gamma$	$-\Delta\Gamma$	0	$Q_G + \Delta Q$	$-\Delta Q$	0
Anticyclonic gyre	$E_G + \Delta E$	$-\Gamma_G + \Delta\Gamma$	$-\Delta\Gamma$	$-Q_G$	ΔQ	$-\Delta Q$	0
Barotropic gyre	$E_G + \Delta E$	$\Gamma_G/2 + \Delta\Gamma$	$\Gamma_G/2 - \Delta\Gamma$	0	$Q_G + \Delta Q$	$-\Delta Q$	Q_G
Seamount	$E_T + \Delta E$	$\Delta\Gamma$	$\Gamma_T - \Delta\Gamma$	0	ΔQ	$-\Delta Q$	0
Bowl	$E_T + \Delta E$	$\Delta\Gamma$	$\Gamma_T - \Delta\Gamma$	0	ΔQ	$-\Delta Q$	0

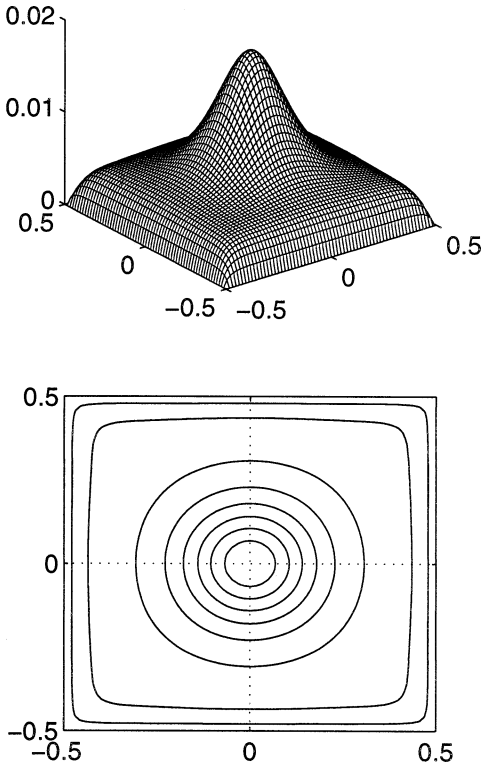

FIG. 7. The temperature anomaly due to penetrative convection throughout the ambient cyclonic gyre shown in Figs. 2 and 3. The surface cooling event is parameterized by $\Delta E = 1.2 \times 10^{-5}$, $\Delta\Gamma = 0.0125$, and $\Delta Q = 0.2$, which implies that $L_T^2 = 0.0625$.

The most probable states of the equilibrium statistical theory for all preconditioned ambient flows and for all convectively forced flows are determined by specifying the values of the parameters listed in Tables 1 and 2 and solving the resulting mean-field equations in (2.10). In particular, the strong surface cooling event for most examples cited in this paper will be parameterized by a single set of parameters: an energy, $\Delta E = 1.2 \times 10^{-5}$, a circulation anomaly, $\Delta\Gamma = 0.0125$, and a potential vorticity anomaly, $\Delta Q = 0.2$. A surface cooling event parameterized by these values will accelerate the dimensional large-scale gyre by a few centimeters per second, which is a reasonable magnitude (Marshall and Schott 1999); otherwise these values are chosen to illustrate the characteristic tendency of thermal and potential vorticity anomalies to congregate in regions of upwelling isopycnal surfaces. Since the length parameter, $L_T = 0.25$, is relatively small, this implies that the initial surface cooling event on average covers a relatively small area. Convective overturning in ambient preconditioned gyres is discussed in section 4 and in topographically induced initial flow in section 5.

4. The preconditioning effect of basin-scale gyres

So how do hetons generated by strong surface cooling events cluster in ambient flows preconditioned by surface wind-driven gyres? Observations suggest that convective overturning in preconditioned cyclonic gyres predominantly occurs in regions of upwelling isopycnal surfaces (Hogg 1973; Madec et al. 1996; Alverson and Owens 1996). In DM we showed that, without any preconditioning, the hetons cluster in the center of the domain—at moderate energies, small deformation radius, and low heton density—forming a central, baroclinic cold temperature anomaly circumscribed by a stabilizing barotropic rim current. In this section we show that preconditioned *cyclonic gyres*, whose isopycnal surfaces dome upwards in the center of the basin, confine the cold-temperature anomaly, circumscribed by a barotropic rim current. However, anticyclonic gyres, whose isopycnal surfaces are depressed in the basin center, and purely barotropic flows, whose isopycnal surfaces are flat throughout the basin, do not confine hetons as the cold-temperature anomalies cluster within the corners and along the edges of the basin.

Convective overturning throughout cyclonic or anticyclonic wind-driven gyres is parameterized by combining the contributions to the total energy, upper- and lower-layer circulation, and potential vorticity extrema due to convection and to the initial ambient flow. The total energy and circulations in each layer are obviously related to the sum of the convective and ambient portions; however, the potential vorticity extrema are also additive: the generation of hetons increases the maximum potential vorticity in the upper layer and decreases the minimum potential vorticity in the lower layer. The net total parameters defining convective overturning in the ambient gyres are summarized in Table 2.

a. Cyclonic gyre

The cyclonic gyre shown in the top row of Fig. 2 is produced as the most probable state of the equilibrium statistical theory given an energy, $E_G = 6.3 \times 10^{-5}$, an upper-layer circulation, $\Gamma_G = 0.07$, and maximum upper-layer potential vorticity in the small-scale field, $Q_G = 2.0$. As described in section 3a, the gyres, produced by sustained wind forcing over the upper layer, have vanishing potential vorticity in the lower layer. The flow for this particular choice of parameter values is rather evenly spread throughout the basin with the energy neither concentrated in the basin center nor isolated in jets pressed against the basin edges. We also note that, despite the vanishing potential vorticity in the lower layer, the energy in the preconditioned flow is more than 97% barotropic. Thus, the energy in the ambient gyre shown in Fig. 2 is approximately five times greater than the energy introduced by convective overturning, discussed in section 3c.

Indeed, the most probable distributions of heat and potential vorticity anomalies in the ambient cyclonic gyre following a surface cooling event defined by parameters given in section 3c are shown in Figs. 7 and 8, respectively. These plots show the *difference* between

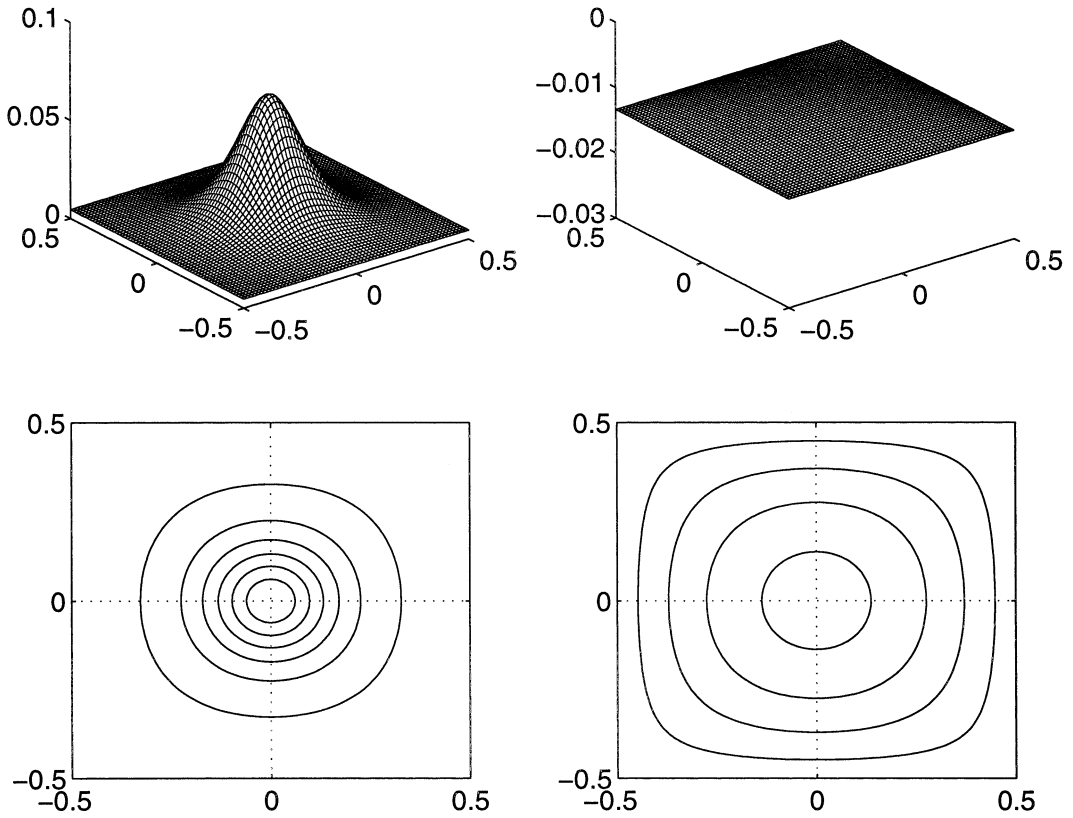

FIG. 8. The distribution of the potential vorticity anomaly in the upper and lower layers, shown in the left and right columns, respectively, due to penetrative convection throughout the preconditioned ambient cyclonic gyre shown in the top rows of Figs. 2 and 3. The surface cooling event is parameterized as in Fig. 7.

the thermal fields and the potential vorticity fields of the most probable states calculated with convective forcing and without. Comparing the thermal anomaly in Fig. 7 to the preconditioned thermal field in the cyclonic gyre in the top row of Fig. 3 shows that hetons tend to cluster in the center of the basin, aligned with the center of the gyre. Although the individual hetons are purely baroclinic structures, an overwhelming portion of the energy in the convectively forced flow—approximately 97%—remains in the barotropic component.

The upper- and lower-layer potential vorticity anomalies, q_1 and q_2, generated by convective overturning in the ambient cyclonic gyre are shown in the left and right columns of Fig. 8. Positive potential vorticity is concentrated in the center of the upper layer of the fluid but negative potential vorticity is dispersed evenly throughout the lower layer. The flow induced by surface forcing therefore tends to strengthen the cyclonic gyre. The overwhelming portion of the energy in the flow is barotropic and, given the broad extent of the induced streamlines, the central cold-temperature anomaly is confined by a barotropic governor.

In Fig. 9 we show the thermal anomaly for the most probable state within the ambient gyre following a surface cooling event parameterized by a very small value, $L_T = 0.07$. This is accomplished by reducing the circulation anomaly generated by surface cooling to $\Delta\Gamma = 0.001$, while retaining the values for energy, $\Delta E = 1.2 \times 10^{-5}$, and the potential vorticity anomaly, $\Delta Q = 0.2$. However, the typical structure produced by the statistical theory—a cold-temperature anomaly circumscribed by a barotropic rim current—is relatively insensitive to the parameter, L_T^2, although smaller values lead to a sharper peak in the predicted thermal anomaly. Additional experiments, not shown here, have explored the effects of the concentration of the gyre, the strength of the heton forcing, and the energy in the heton ensemble. In all cases the general structure of the most probable states of the heat and potential vorticity following convective overturning in ambient cyclonic gyre is the same as that reported here.

b. Anticyclonic gyre

The anticyclonic gyre shown in the middle row of Fig. 2 is produced as the most probable state of the equilibrium statistical theory given an energy, $E_G = 6.3 \times 10^{-5}$, an upper-layer circulation, $-\Gamma_G = -0.07$, and minimum upper-layer potential vorticity in the small-scale field, $-Q_G = -2.0$. The flow here is identical to the cyclonic gyre investigated in section 4a except for the rotational sense of the gyre. The flow for this par-

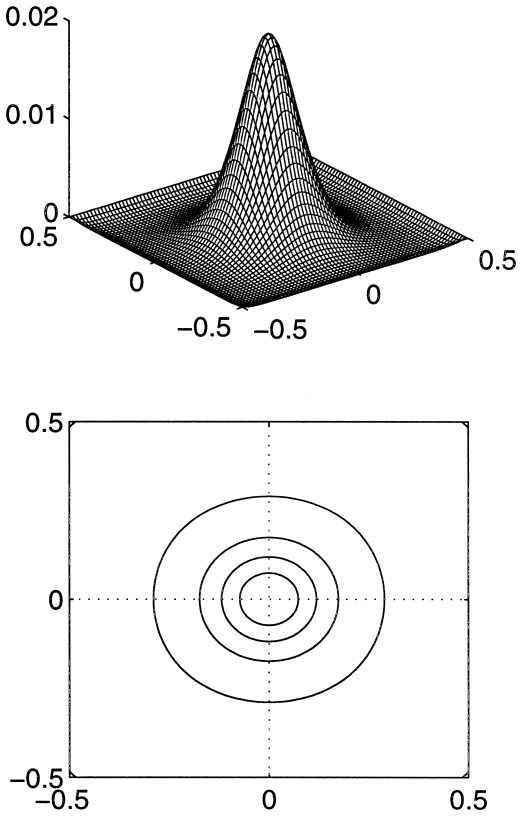

FIG. 9. As in Fig. 7 but with a surface cooling event parameterized by $\Delta\Gamma = 0.001$ and $L_T = 0.07$.

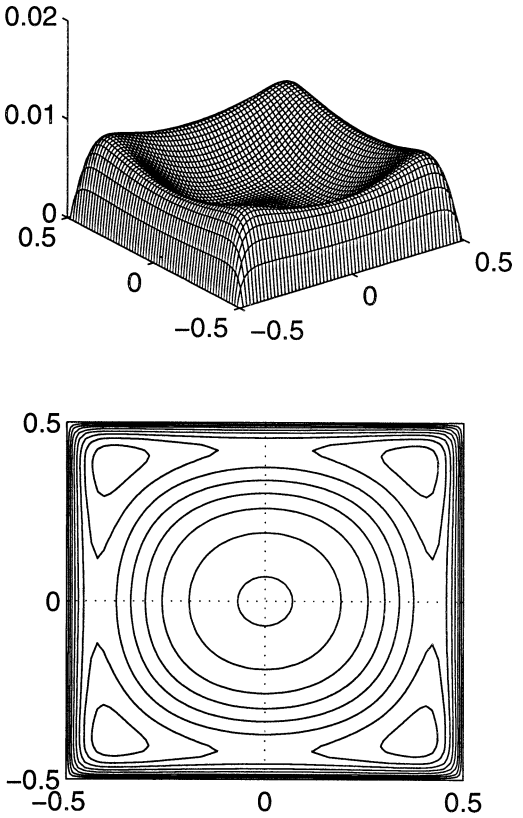

FIG. 10. The temperature anomaly due to penetrative convection throughout the preconditioned ambient anticyclonic gyre shown in the middle rows of Figs. 2 and 3. The surface cooling event is parameterized as in Fig. 7.

ticular choice of parameter values is rather evenly spread throughout the basin with the energy neither concentrated in the basin center nor isolated in jets pressed against the basin edges. We also note that, despite the vanishing potential vorticity in the lower layer, the energy in the preconditioned flow is more than 97% barotropic.

The thermal anomaly generated by convective overturning in the ambient anticyclonic gyre following a surface cooling event defined by the parameters discussed in section 3c is shown in Fig. 10. Hetons avoid the basin center and tend to cluster within the corners and along the edges of the square domain. The distribution of heat in the convectively forced anticyclonic gyre is very different from the distribution in the ambient cyclonic gyre discussed in section 3a: the anticyclonic gyre obviously does not confine hetons to the center of the domain.

For the anticyclonic gyre, the positive potential vorticity introduced in the upper layer by convective overturning is concentrated in the corners and along the edges of the basin. The negative potential vorticity introduced in the lower layer is dispersed evenly throughout the basin. The flow induced by convective overturning therefore tends to strengthen the preexisting anticyclonic gyre. In one sense, the behavior of convective overturning in the ambient anticyclonic gyre is similar to the behavior in the ambient cyclonic gyre: positive potential vorticity anomalies collect near the regions of upwelling in the preconditioned fluid interface. For the anticyclonic gyre this region of upwelling lies along the basin edges, and the hetons in the convectively forced flow are not confined to the center of the basin. Of course, in actual ocean basins other physical boundary layer currents, not accounted for in the basic inviscid model, can introduce other effects that swamp the weak boundary upwelling predicted here.

c. Barotropic gyre

In sections 4a and 4b we showed that the position of the fluid interface in the preconditioned ambient gyres exerts a powerful influence on the distribution of heat and potential vorticity following a strong surface cooling event. Might this result, however, depend on the rotational sense of the ambient flow rather than the upwelling or downwelling of the isopycnal surfaces? In this section we show that the most probable distribution of hetons is not solely controlled by the rotational sense of the ambient flow. The isopycnal surfaces in purely barotropic flows, which may rotate in either a cyclonic or anticyclonic sense, are flat throughout the basin.

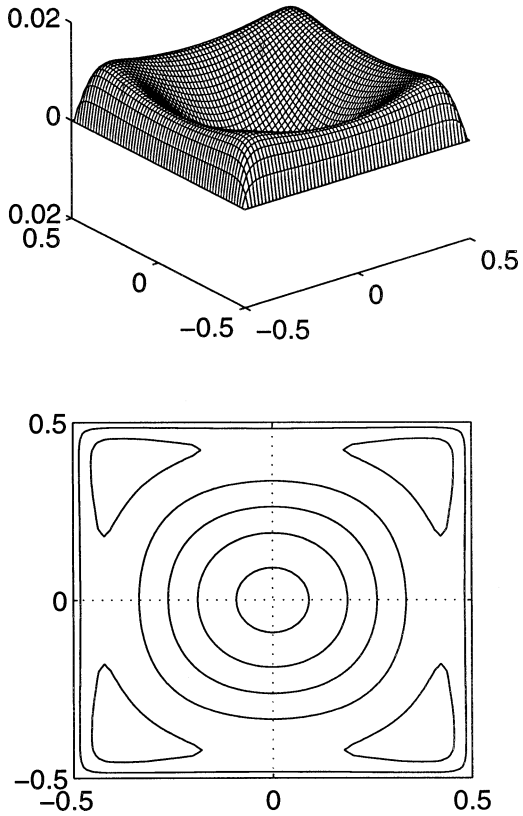

FIG. 11. The temperature anomaly due to penetrative convection throughout the preconditioned ambient barotropic cyclone shown in the bottom rows of Figs. 2 and 3. The surface cooling event is parameterized as in Fig. 7.

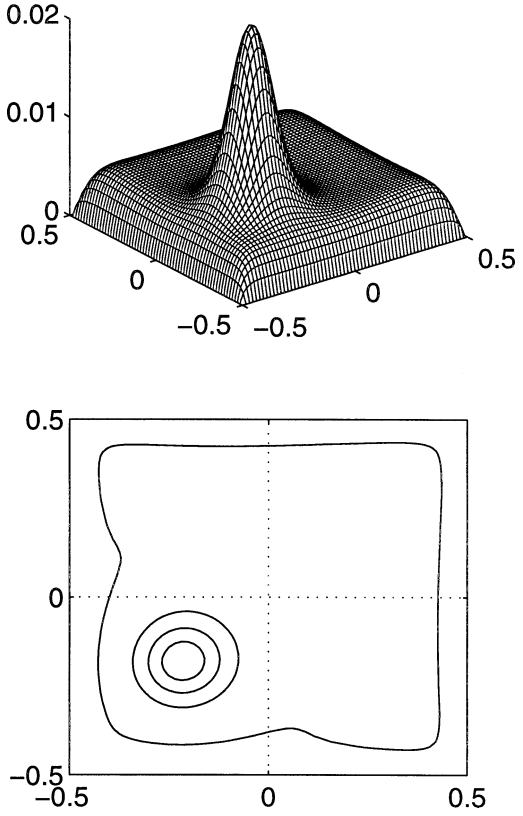

FIG. 12. The temperature anomaly due to penetrative convection throughout the preconditioned flow induced by the localized seamount shown in Figs. 4 and 5. The surface cooling event is parameterized as in Fig. 7.

However, we show that, for a surface cooling event of the same magnitude as in sections 4a and 4b, the hetons seeded in a cyclonic ambient barotropic flow are *not confined* by the large-scale barotropic circulation but tend to collect near the sides of the basin. Also, hetons are not confined by barotropic anticyclones either, a result that is not shown here.

The energy, total circulation, and potential vorticity extrema in the ambient barotropic cyclone is unchanged from the cyclonic and anticyclonic gyres, with $E_G = 6.3 \times 10^{-5}$, $\Gamma_G = 0.07$, and $Q_G = 2.0$. The ambient flow, shown in the bottom row of Fig. 2, is also produced as the most probable state of the equilibrium statistical theory described in section 2b. The flow is rather evenly spread throughout the basin and bears a strong resemblance to the cyclonic gyre, shown in the top row of Fig. 2. However, the flow in the purely barotropic cyclone contains no baroclinic part and the fluid interface that separates the two layers is flat.

The thermal anomaly introduced into an ambient barotropic cyclone following a surface cooling event is shown in Fig. 11. The thermal anomaly is raised near the boundary of the basin, which shows that hetons tend to cluster near the edges and corners of the square domain. Despite the striking visual similarity in the large-scale flow fields, the distribution of heat in the convectively forced purely barotropic cyclone is very different to the distribution in the ambient cyclonic gyre discussed in section 4a: the purely barotropic cyclone does not confine hetons to the center of the domain.

We have shown here that a purely barotropic cyclone with the same surface cooling event fails to confine hetons in a manner consistent with observations. Purely barotropic anticyclones do not confine hetons, either. In fact, barotropic anticyclones defined by comparable parameters as the barotropic cyclones produce identical temperature anomalies following strong surface cooling events—defined by the parameters in section 3c—a prediction that shows the irrelevance of the rotational sense of the ambient flow. As reported earlier in DM, there is a preconditioning effect of barotropic gyres with maximal values of the patchiness parameter, L_T; with the low to moderate values of L_T considered in this paper, there is no such tendency. The differences between the conclusions drawn here and in Legg and Marshall (1998), which found that barotropic preconditioned flow constrains the spread of convective overturning, may be due to the difference in forcing: in Legg and Marshall (1998) the convective forcing is localized in space,

whereas here it is spread homogeneously throughout the basin.

5. Topographic preconditioning for the spreading phase

In section 4 we showed that the most probable distributions of heat and potential vorticity following a basinwide surface cooling event is strongly dependent on the preconditioning of the isopycnal surfaces of the ambient flow. Hetons tend to cluster in the center of the basin, confined by a barotropic governor within preconditioned cyclonic gyres, whose isopycnal surface domes *upward* in the center of the basin. In this section we investigate the effects of adding hetons to *topographically* preconditioned flows, including the localized, upwelling seamount shown in the left-hand column of Fig. 4, and the broad basinwide depression of the asymmetric bowl shown in the right-hand column of Fig. 4.

As described in section 3b, the topographically preconditioned flows possess vanishing potential vorticity in both upper and lower layers. However, due to the nontrivial bottom topography, there are nonzero values of energy, E_T, and circulation, Γ_T, in the lower layer of the ambient flow. In a manner similar to the gyres described in section 4, convective overturning throughout these topographically preconditioned flows is also captured by adding the contributions to the total energy, circulations, and potential vorticity extrema due to the convective forcing and to the ambient flow. This combination is summarized in the bottom section of Table 2.

Here, the preconditioned thermal field is again the critical variable. For the ambient flow induced by the localized seamount, which revolves anticyclonically about the raised isopycnals, hetons tend to cluster just above the topographic peak. For the cyclonic ambient flow induced by the bowl, however, the cold-temperature anomalies tend to congregate in the corners of the basin domain, raising the fluid interface in the corner farthest from the topographic minimum.

a. Seamount

The localized seamount, shown in the lower left-hand corner of Fig. 4, is defined in section 3b with height, $H = 0.36$, and width, $w = 0.125$, which is 2.5 times as large as the Rossby deformation radius, $L_\rho = 0.05$. The energy in the ambient flow induced by the bottom topography is approximately half the energy in the gyres, $E = 3.7 \times 10^{-5}$, and the lower-layer circulation is $\Gamma_2 = -0.0342$. The fluid interface follows the topography, rising over the Gaussian seamount. Whereas upwelling isopycnal surfaces are associated with cyclonic flow in the gyre as discussed in section 3a, here upwelling topography, which also displaces the isopycnals upward, induces anticyclonic flow about the peak. The energy in the ambient flow about the seamount lies predominantly in the barotropic component—approximately 95%—with the flow concentrated about the seamount peak.

The most probable arrangements of heat and potential vorticity anomalies following a surface cooling event defined by the parameters given in section 3c are presented in Figs. 12 and 13. The cold-temperature anomaly in Fig. 12, when compared to the ambient flow about the seamount shown in the left column of Fig. 6, shows that hetons tend to cluster about the peak of the seamount. Although the hetons are purely baroclinic structures, an overwhelming portion of the energy—approximately 94%—remains in the barotropic component in the most probable state of the convectively forced flow predicted by the statistical theory.

The potential vorticity anomaly in the upper and lower layers generated by convective overturning following strong surface cooling over ambient flow induced by the Gaussian seamount is shown in Fig. 13. The potential vorticity vanishes in both layers in the ambient flow. The convection concentrates negative potential vorticity in the lower layer in the region immediately above the seamount but evenly disperses positive potential vorticity throughout the upper layer. Notice that this is nearly opposite to the distribution of potential vorticity introduced into the preconditioned cyclonic gyre discussed in section 4a. This distribution of potential vorticity tends to strengthen the anticyclonic flow about the seamount. Thus, the cold-temperature anomaly that forms above the highest peak in the topography is confined by a strengthened anticyclonic flow, with a predominant portion of energy in the barotropic component.

A dramatic example of hetons congregating above upwelling topography is shown in the thermal field depicted in Fig. 14. The surface cooling event is quite intense in this example, with a circulation anomaly, $\Delta\Gamma = 0.01$, heton strength, $\Delta Q = 1.8$, and energy, $\Delta E = 1.2 \times 10^{-5}$. The length scale, $L_T = 0.07$, implies that, in an averaged statistical sense, only a small portion of the domain is seeded with hetons. In fact, the thermal field shown in Fig. 14 forms a sharp peak in the lower left-hand corner of the basin, just above the peak of the seamount. Additional experiments, not shown here, have explored the effects of the height, width, and placement of the seamount, which changes the energy and strengths of the anticyclonic flow about the upwelling topography. In all cases the heat and potential vorticity introduced by convective overturning is concentrated above the peak of the seamount.

b. Bowl

The basinwide bowl topography shown in the right column of Fig. 4 induces a large-scale cyclonic flow, shown in the bottom row of Fig. 5. The lowest point in the topographical depression is displaced toward the lower left-hand corner of the square domain and the

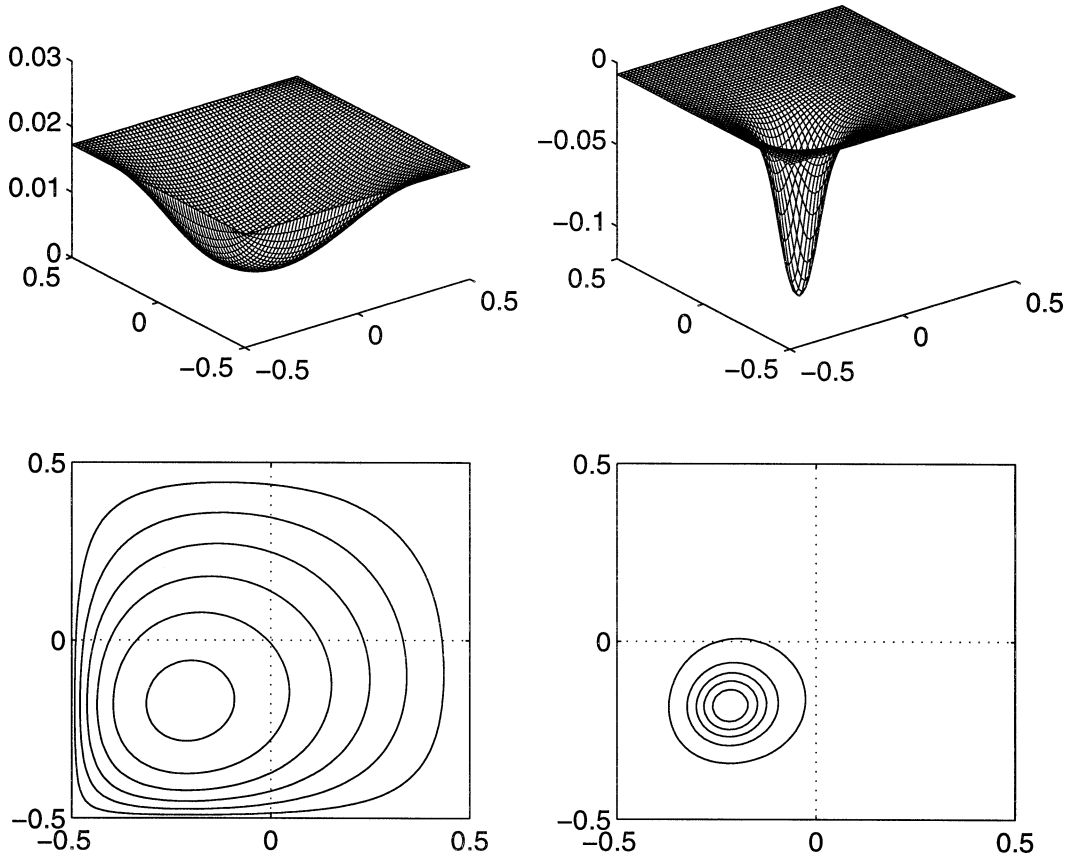

FIG. 13. The distribution of the potential vorticity anomaly in the upper and lower layers, shown in the left-hand and right-hand columns, respectively, due to penetrative convection throughout the preconditioned flow induced by the localized seamount shown in Figs. 4 and 5. The surface cooling event is parameterized as in Fig. 7.

depth of the bowl, $H = -0.1$, is chosen so that the energy in the ambient flow, $E = 3.6 \times 10^{-5}$, matches the energy induced by the seamount. The circulation in the lower layer is $\Gamma_2 = 0.0439$. The flow is rather evenly spread throughout basin with approximately 98% of the energy in the barotropic component.

Hetons introduced into ambient flow over the basinwide bowl tend to avoid the deepest parts of the basin. The thermal field induced by a surface cooling event defined by the parameters described in section 3c is shown in Fig. 15. The cold-temperature anomaly, when compared to the ambient topographically induced flow in the left column of Fig. 6, shows that hetons tend to cluster near the sides and corners of the basin. In fact, the fluid interface is raised by the greatest amount in the upper right-hand corner, which is farthest from the topographic minimum. However, the maximum height of the displaced interface over topographic depressions is smaller than the maximum height over topographic upwellings. We also note that there is a weaker secondary concentration of hetons in the very center of the basin, displaced slightly toward the topographic minimum. For energy larger than the value presented here, this concentration increases and moves toward the basin center; for smaller values of energy the hetons do not congregate in the domain center at all.

The potential vorticity anomalies in the upper and lower layers, not shown, following convective overturning in the ambient flow induced by the asymmetric bowl tend to reinforce the preexisting cyclone. The potential vorticity vanishes in both layers in the ambient flow. The introduction of hetons in the domain concentrates positive potential vorticity in the center of the basin and evenly disperses negative potential vorticity throughout the lower layer. The topographically preconditioned cyclonic gyre therefore tends to push the hetons toward the edges of the basin, an effect that has been reproduced for a wide range of ambient flow and heton parameter values.

6. Composite preconditioning with gyres and topography

Two of the prototype preconditioned flows introduced in sections 4 and 5—the cyclonic wind-driven gyre and the anticyclonic flow induced by upwelling topography—locally confine the heat and potential vorticity introduced by convective overturning that follows a bas-

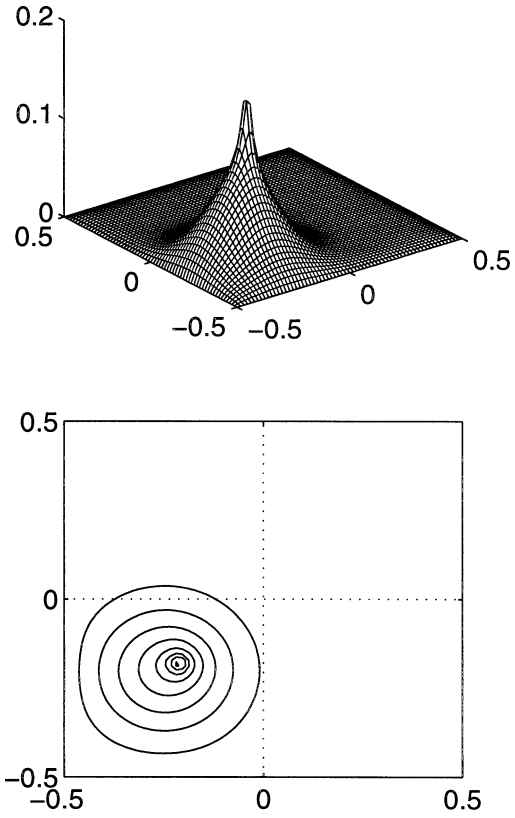

FIG. 14. The thermal field following a strong and sparse surface cooling event over ambient flow induced by the localized seamount. The convective overturning is parameterized by $\Delta E = 1.2 \times 10^{-5}$, $\Delta\Gamma = 0.01$, and $\Delta Q = 1.8$.

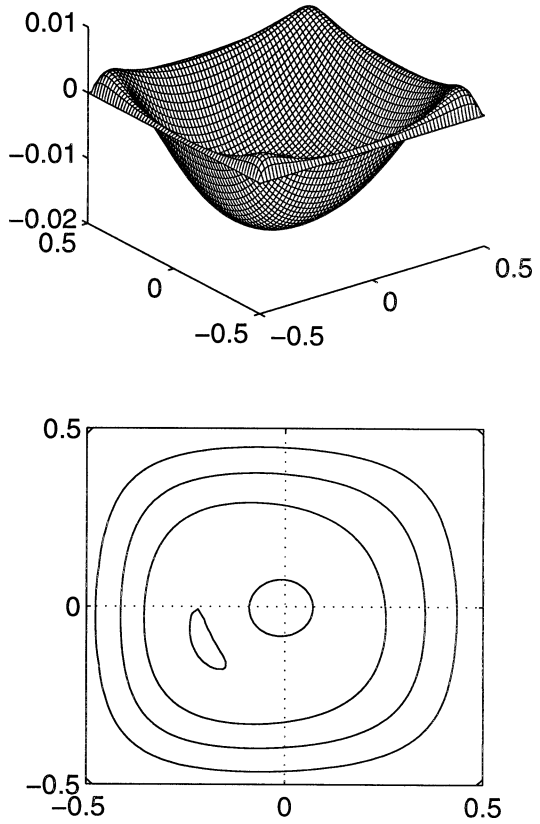

FIG. 15. The thermal field following a surface cooling event over ambient flow induced by the basinwide bowl shown in Figs. 4 and 5. The surface cooling event is parameterized as in Fig. 7.

inwide surface cooling event. In the ambient wind-driven cyclonic gyre, which is discussed in section 3a, the cold-temperature anomaly and the positive potential vorticity in the upper layer are both concentrated within the peak of the upwelling isopycnal surface located in the center of the gyre. In the anticyclonic flow about the seamount, which is discussed in section 3b, the cold-temperature anomaly and the negative potential vorticity in the lower layer are localized within the raised isopycnals that lie directly above the peak of the topography. In this section we address the following question: how do heat and potential vorticity congregate within ambient flow preconditioned by both wind-driven and topographic elements, each of which raise the isopycnal surfaces but establish vortical flows that rotate in opposite senses?

In order to carefully separate the contributions from each of these elements, we ''grow'' a sequence of increasingly larger seamounts within an established cyclonic gyre with a given energy and upper-layer circulation that models the large-scale flow induced by surface wind stress. We find that even small seamounts exert a strong influence on the preexisting gyre: the cyclonic circulation generally avoids the region of bottom upwelling and strengthens the flow in the remainder of the basin. Larger seamounts, which control a significant portion of the energy in the flow, induce a local anticyclonic flow about the topographic peak. However, although tall seamounts introduce large displacements of the fluid interface above the topographic peak, the induced displacement is usually greater within the center of the gyre. Thus, the statistical theory predicts that hetons, which model the convective overturning produced by surface cooling using the same parameters provided in section 3c, preferentially congregate within the center of the gyre with very little of the heat and potential vorticity confined above the seamount.

a. Composite ambient flow cyclonic gyre and upwelling seamount

We replace the flat bottom of the cyclonic gyre investigated in section 4a, defined by potential vorticity extremum $Q_G = 2.0$, upper-layer circulation $\Gamma_G = 0.07$, and energy $E_G = 6.3 \times 10^{-5}$, with a sequence of localized Gaussian seamounts with height H increasing from $H = 0.1$ to a maximum of $H = 0.36$. The width and location of the seamount is identical to the topography described in section 3b—in each case the peak

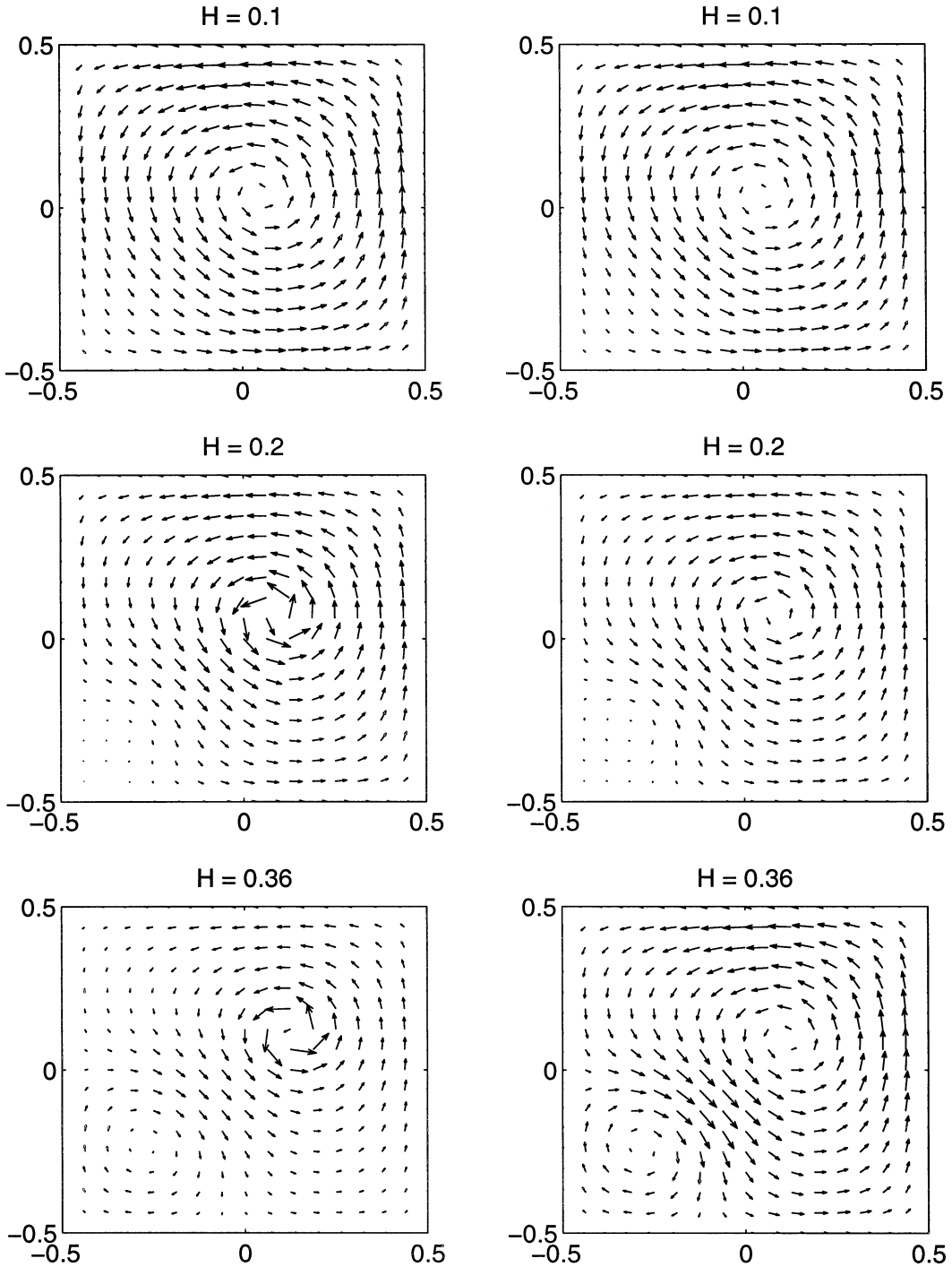

FIG. 16. Upper- and lower-layer velocity fields, located in the left- and right-hand columns, respectively, for the composite ambient flow consisting of a wind-driven cyclonic gyre, parameterized as in Fig. 2, and a localized seamount with height $H = 0.1$ (top), 0.2 (middle), and 0.36 (bottom).

of the topography is centered about the point $(-0.25, -0.235)$ and the width of the Gaussian profile is given by $w = 0.125$, which is two and a half times larger than the Rossby radius of deformation. In order to account for the nontrivial bottom topography, we increase the total energy and lower-layer circulation to account for the portion of the flow due to the seamount. From the results in section 5a we have shown that a seamount with height $H = 0.36$ induces a flow with bottom-layer circulation $\Gamma_T = -0.046$, and energy $E_T = 3.6 \times 10^{-5}$.

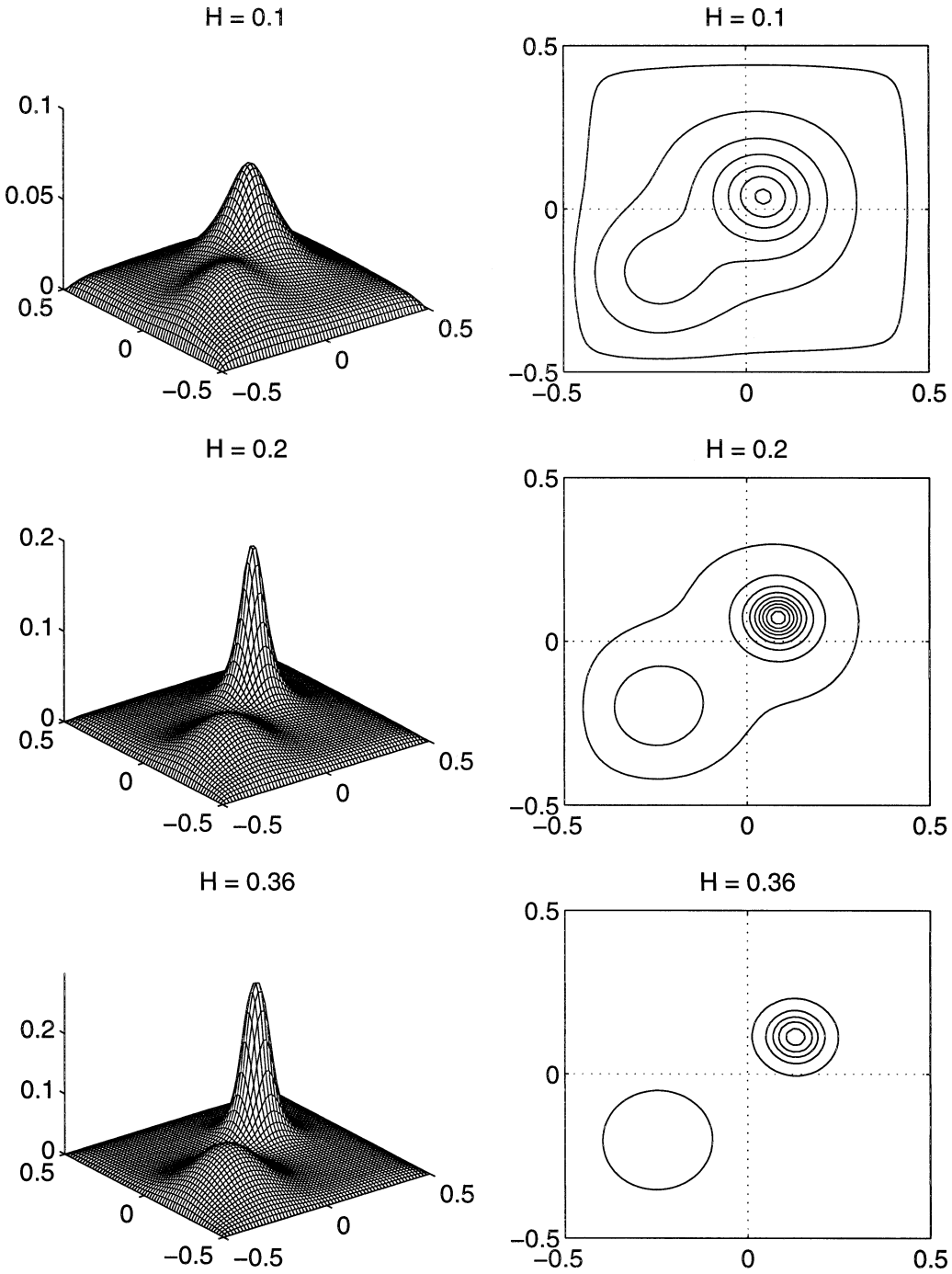

FIG. 17. The preconditioned thermal field in the composite ambient flow consisting of a wind-driven cyclonic gyre, parameterized as in Fig. 2, and a localized seamount with height $H = 0.1$ (top), 0.2 (middle), and 0.36 (bottom).

For ''growing'' topography the energy scales quadratically with height, and the circulation linearly.

In Fig. 16 we show the velocity fields produced as the most probable state of the equilibrium statistical theory for three composite flows with both wind-driven gyres and nontrivial bottom topography given by seamounts with height $H = 0.1$, 0.2, and 0.36 in the top, middle, and bottom rows, respectively. For these three examples the energy, E_T, in the topographically induced flow is taken to be $E_T = 0.3 \times 10^{-5}$, 1.1×10^{-5}, and 3.6×10^{-5}, and the lower-level circulation is $\Gamma_T = -0.013$, -0.026, and -0.046, respectively. By comparing the flow patterns shown in Fig. 16 to the case with trivial bottom topography shown in the upper row

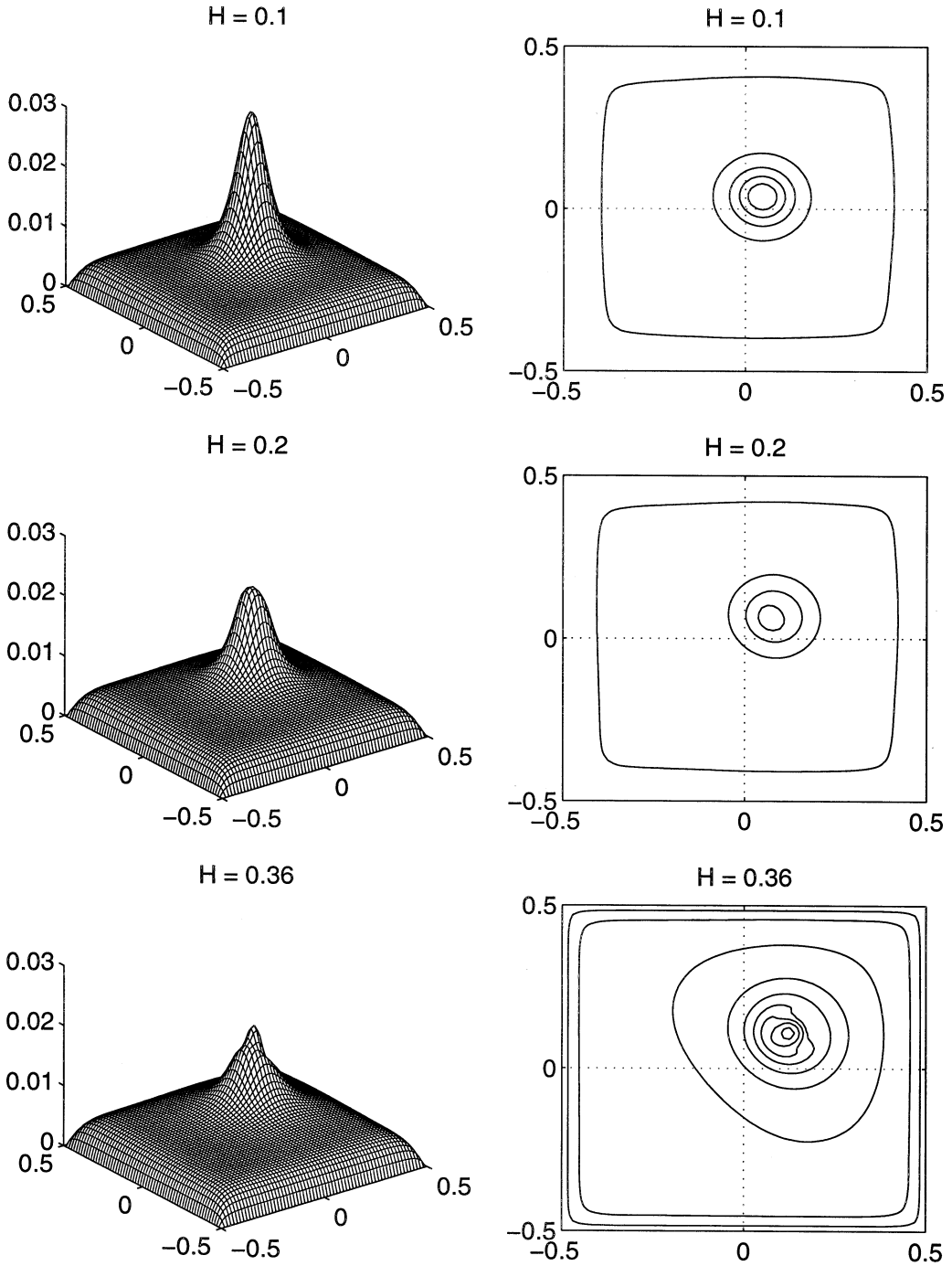

FIG. 18. The thermal anomaly following a surface cooling event over the composite ambient flow consisting of a wind-driven cyclonic gyre, parameterized as in Fig. 2, and a localized seamount with height $H = 0.1$ (top), 0.2 (middle), and 0.36 (bottom). The surface cooling event is parameterized as in Fig. 6.

of Fig. 2, we see that even the smallest seamount displaces the position of the cyclonic gyre, which tends to concentrate the flow away from the topographic upwelling. In the case with the smallest hill the cyclonic gyre sweeps over the slight upwelling, and the velocity field contains no anticyclonic rotation. As the seamount increases in height, however, anticyclonic flow is established over the peak of the topography, while the cyclonic gyre is concentrated in the opposite corner. Although the flow has a large barotropic component—the barotropic portion of the energy decreases only to 91% for the case with $H = 0.36$—a baroclinic signature

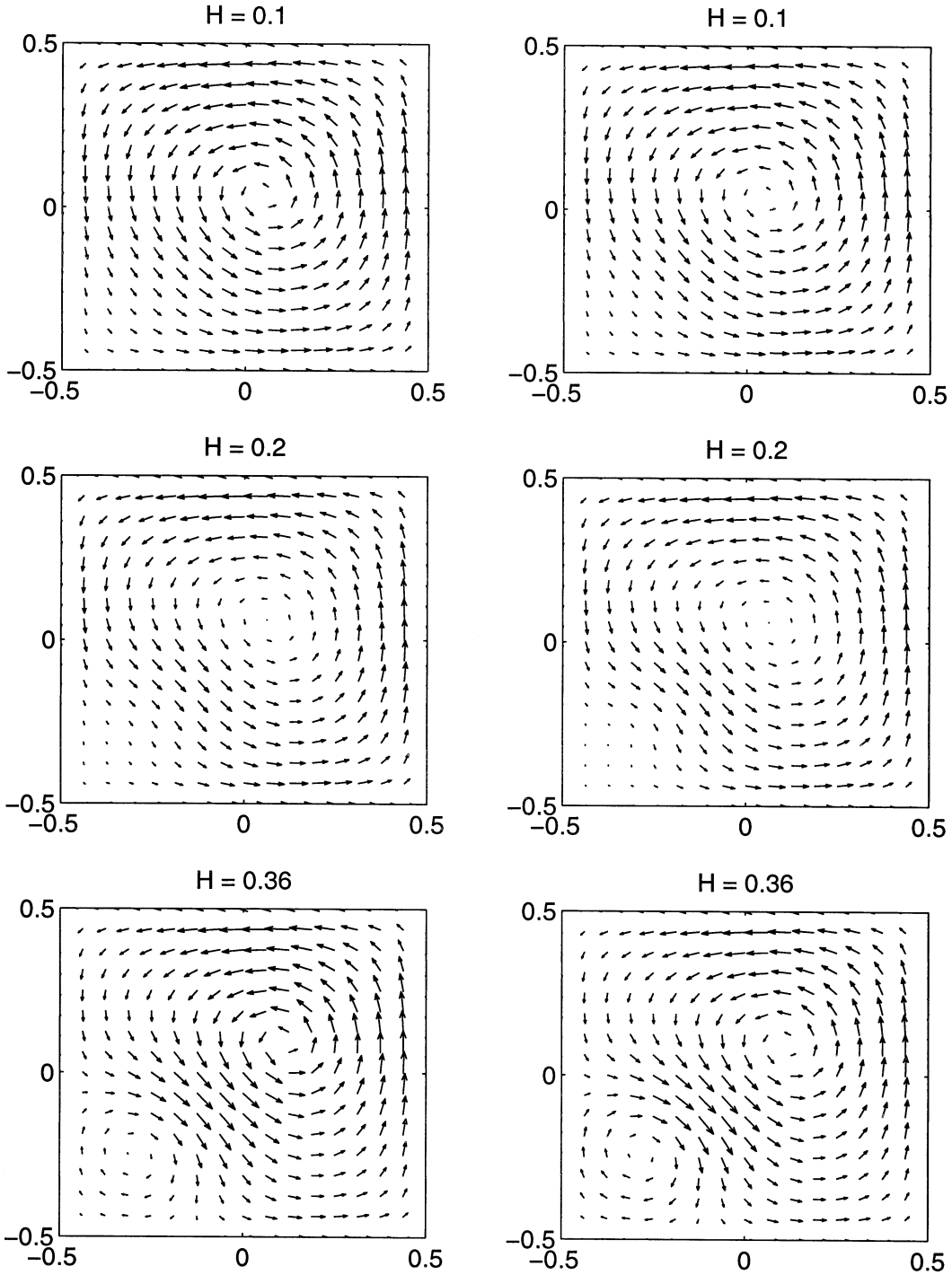

FIG. 19. As in Fig. 16, except for a more evenly distributed ambient gyre, parameterized by $E_G = 6.3 \times 10^{-5}$, $\Gamma_G = 0.09$, and $Q_G = 2.0$.

in the velocity field is apparent through the stronger upper-level flow in the cyclonic gyre and a slightly stronger lower-level flow in the anticyclonic flow above the seamount.

The preconditioned thermal fields for these three composite flows are shown in Fig. 17. In each of these surface plots the cold-temperature concentration due to the topography, which appears in the lower left-hand corner, increases roughly linearly with respect to the height (note the changing scale of the vertical axis). However, the presence of even modest topography strongly alters the thermal field associated with the cy-

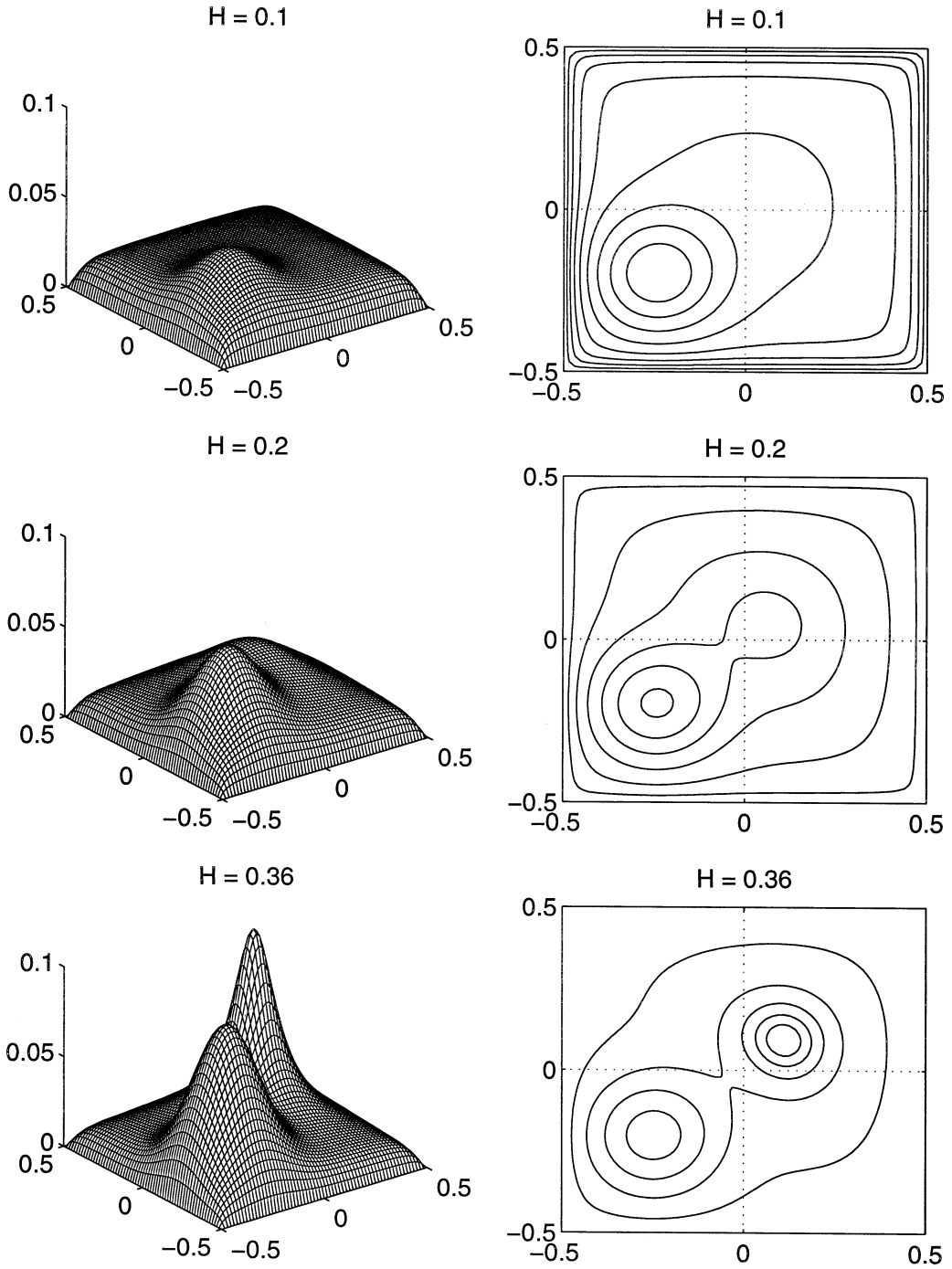

FIG. 20. As in Fig. 17 except for a more evenly distributed ambient gyre parameterized by $E_G = 6.3 \times 10^{-5}$, $\Gamma_G = 0.09$, and $Q_G = 2.0$.

clonic gyre. The slope of the thermal field for the cyclonic gyre with trivial topography rises gently (see the top row of Fig. 3); however, in the composite flow the cold-temperature thermal field associated with the gyre avoids the region that contains the upwelling seamount and forms a sharp peak in the opposite quadrant. In each of the sequences selected, the upwelling of the isopycnal surface associated with the gyre dominates the upwelling that follows the seamount. Furthermore, the upper-layer potential vorticity, which is rather evenly dispersed in the example with a flat bottom, also congregates in the center of the gyre.

What happens when a basinwide surface cooling event generates hetons in these composite flows? The

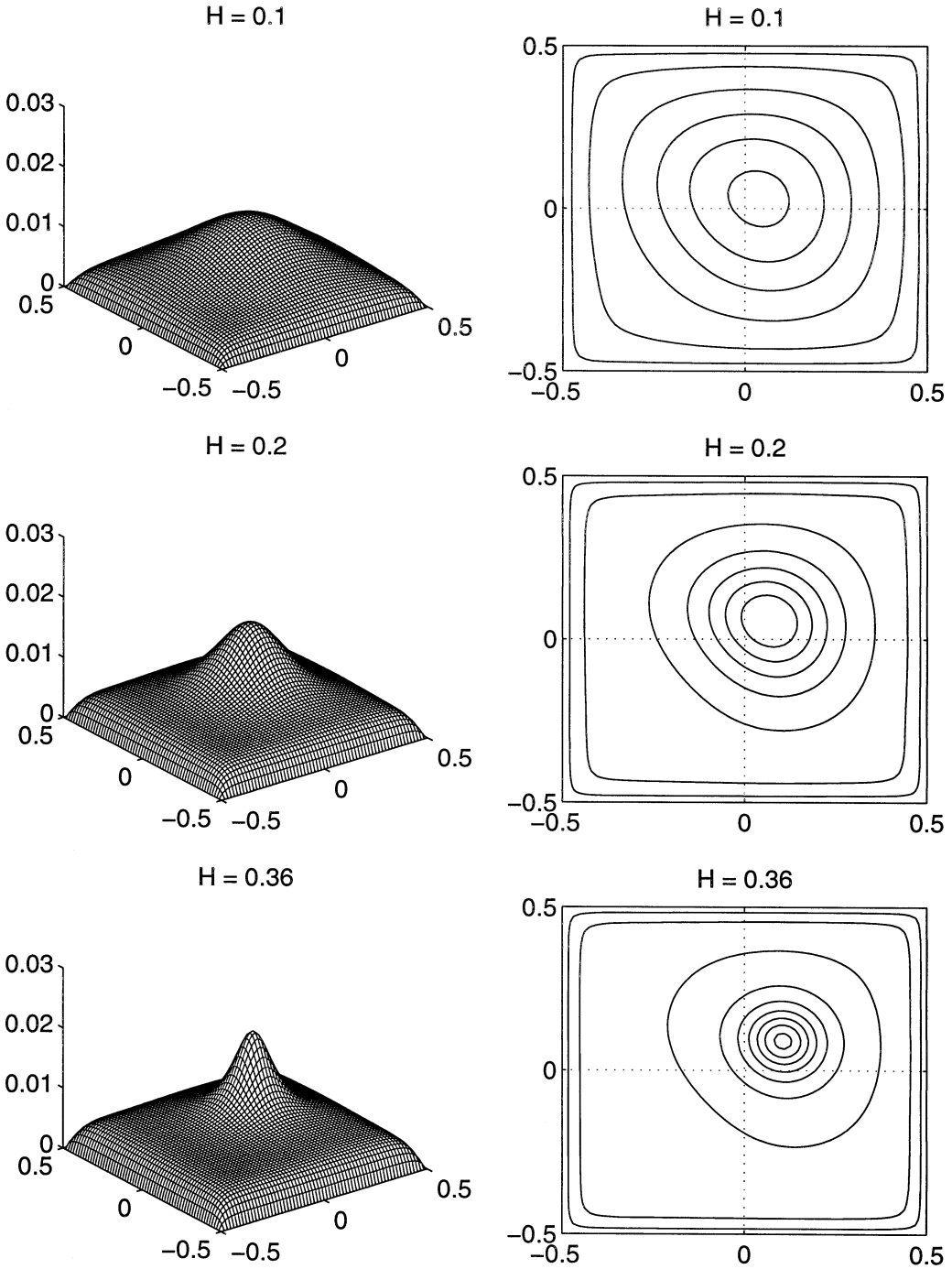

FIG. 21. As in Fig. 18 except for a more evenly distributed ambient gyre parameterized by $E_G = 6.3 \times 10^{-5}$, $\Gamma_G = 0.09$, and $Q_G = 2.0$.

equilibrium statistical theory predicts that the cold-temperature anomaly and potential vorticity lie almost exclusively within the cyclonic gyre, with practically no congregation of either heat or PV collecting above the seamount. In Fig. 18 we show thermal anomalies introduced by convective overturning in each of the three composite flows with $H = 0.1$, 0.2, and 0.36. In these experiments the convective overturning is parameterized by the values provided in section 3c, that is, maximum potential vorticity anomaly $\Delta Q = 0.2$, circulation anomaly $\Delta\Gamma = 0.0125$, and energy $\Delta E = 1.2 \times 10^{-5}$. These parameters match the values used to capture the

basinwide surface cooling in the prototype wind-induced gyres and topographic flows discussed in sections 3 and 4, respectively.

In each of the plots shown in Fig. 18 the cold-temperature anomaly is located directly within the center of the cyclonic gyre, which moves toward the upper left-hand corner of the domain as the topography becomes larger. However, even as the hetons are preferentially distributed within the increasingly tight gyre, the cold-temperature anomaly is, paradoxically, broader and somewhat less confined by flow induced by the largest seamount. Notice, finally, that there is no trace of hetons over the seamount, which is located in the bottom left-hand corner of the diagram, in any of these examples.

b. *Composite ambient flow with ''relaxed'' cyclonic gyre*

In section 6a, we showed that hetons preferentially collect in the center of the gyre with no discernible congregation above the seamount. In this section we alter the ambient cyclonic gyre—spreading the flow more evenly throughout the domain by increasing the circulation in the upper layer—in an attempt to tip the balance in favor of the topographic upwelling. However, we find that in all cases for the strength of the surface cooling event that we consider, for both dispersed and tightly confined gyres, the cyclonic gyre collects nearly all of the cold-temperature and potential vorticity anomalies that are produced by convective overturning. Furthermore, other experiments, not reported in detail here, show that there are two branches of solutions, each of which solves the mean-field equations in (2.10) for any given preconditioned gyre and seamount: 1) one in which the hetons congregate within the center of the gyre and 2) one in which the hetons are found directly atop the topographic peak. For all cases in which the gyre contains even a moderate portion of the energy—say, 10%—the hetons are more likely to be found within the gyre than over the seamount in the sense that this branch of solutions has the higher entropy.

In this section the prototype cyclonic gyre, over trivial topography, is defined by potential vorticity extremum $Q_G = 2.0$, upper-layer circulation $\Gamma_G = 0.09$, and energy $E_G = 6.3 \times 10^{-5}$. The energy in the flow over trivial topography, not shown, is concentrated within a narrow jet that travels along the edges of the domain. As we ''grow'' a seamount in the lower left quadrant of the domain, with heights $H = 0.1$, 0.2, and 0.36 as in section 6a, the gyre is displaced toward the opposing quadrant with a central cyclonic core whose strength increases with taller seamounts. The main difference between the preconditioned flows examined here and the similar composite flow discussed in section 6a is due to the slight increase in circulation in the upper layer, which causes the flow to be more evenly distributed over the domain for comparable magnitudes of topography. The portion of the energy and lower-layer circulation in the flow that is induced by the localized seamount is identical to the values provided in section 6a.

In Fig. 19 we show the composite preconditioned velocity fields for surface wind-forced cyclonic gyres over the localized seamounts with height $H = 0.1$, 0.2, and 0.36. As in section 6a, the portion of the energy that is due to the topographic forcing increases from approximately 10% for the smallest seamount to nearly 40% for the tallest. For very small topography, the cyclonic gyre sweeps over the slight upwelling, and the velocity field contains no anticyclonic rotation. However, even a small seamount induces effects on the large-scale gyre that are quite noticeable: the seamount ''pushes'' the flow toward the opposite corner, transforming the boundary current into a flow whose energy is rather evenly distributed throughout the basin. For the larger seamounts anticyclonic flow patterns are established over the topographic peaks and the cyclonic gyre is more active core, although the strength and baroclinicity of the flow is weaker in the very center of the gyre than the case examined in section 6a.

The preconditioned thermal fields for these composite flows are shown in Fig. 20. By increasing the upper-layer potential vorticity in the cyclonic gyre, we have, for the smaller seamounts given by $H = 0.1$ and 0.2, achieved our aim: the isopycnal surfaces reach a maximum above the topographic peak. For the largest seamount, however, the gyre has concentrated to a sufficient degree that the displacement of the isopycnal surfaces is dominated by the gyre.

How does this affect the most probable distribution of hetons produced by basinwide surface cooling? As in section 6a, the cold-temperature and potential vorticity anomalies are confined within the center of the gyre, even for the cases in which the maximum of the isopycnal surface is located above the seamount. This is shown in the top two rows of Fig. 21, which depicts the distribution of the cold-temperature anomaly due to convective overturning. The peak of the anomaly is aligned with the center of the gyre, which moves toward the upper left-hand corner of the basin as the height of the seamount increases. Also, in contrast to the gyre studied in section 6a, the peak in the cold-temperature anomaly is more pronounced in the flows preconditioned by larger seamounts.

7. Conclusions

We have adapted an equilibrium statistical model for open-ocean convection, first introduced in DM for quiescent initial flow, to account for both nontrivial topographic features, including upwelling seamounts and basinwide depressions and sustained surface wind forcing, which yields large-scale cyclonic and anticyclonic gyres. In the equilibrium statistical model, developed within the context of a two-layer quasigeostrophic fluid, both the prototype ambient flows and the deformation-

scale features of widespread convective overturning are parameterized by a few bulk conserved quantities, such as energy, circulation, and potential vorticity extrema, that capture the essential physical processes in the oceanographic phenomena.

The critical element of the prototype ambient flows, each initially treated separately with no convective forcing from a surface cooling event, is the position of the fluid interface that separates the upper and lower layers, that is, the preconditioned thermal field. For the wind-driven ambient gyres, which are investigated in section 4, the sense of rotation determines the position of the fluid interface: the isopycnal surfaces are raised in the center of the cyclonic gyre, but are depressed in the center of the anticyclonic gyre. We also treat a purely barotropic cyclone in which the fluid interface is flat. For the topographically induced flows, which are investigated in section 5, the isopycnal surfaces generally follow the undulations of the bottom surface: the isopycnals are raised above the upwelling seamount and are pulled downward above the basinwide depression.

Within each of the prototype ambient flows we have provided an identical set of parameters for the energy, circulation, and potential vorticity anomalies that model convective overturning that follows a basinwide surface cooling event. The signature of open-ocean convection—a central cold-temperature anomaly circumscribed by a predominantly barotropic rim current—is observed in the prototype ambient flows with raised isopycnals (Marshall and Schott 1999). We find that the equilibrium statistical theory predicts a cold-temperature core above the upwelling seamount and within the cyclonic gyre, at the very peaks of the preconditioned isopycnal surfaces. Furthermore, the potential vorticity anomalies introduced by convective overturning reinforce the rotational sense of the basic flow: a slight congregation of positive potential vorticity appears in the upper layer of the cyclonic gyre and a slight congregation of negative potential vorticity appears in the lower layer above the seamount, which strengthens the anticyclonic flow about the topographic peak. These predictions of the statistical theory are in accordance with observations in which convective overturning is preferentially observed over large upwelling seamounts and above the raised isopycnals in the center of preconditioned cyclonic gyres (Hogg 1973; Madec et al. 1996; Alverson and Owens 1996). This basic structure also emerges within direct numerical simulation of simple point-vortex heton models, where localized surface cooling leads to a rough balance between buoyancy lost at the surface and the buoyancy gained internally through the lateral propagation of hetons (Legg and Marshall 1998).

The temperature and potential vorticity anomalies are much weaker and tend to collect near the basin edges in the ambient flow induced by downwelling topography and in the anticyclonic gyre and purely barotropic flow. However, there are many competing boundary effects in real ocean flow, due in part to strong boundary currents and shallow continental shelves, that are not considered in the equilibrium statistical theory. All of these considerations taken together support the inefficiency of both downwelling topography and anticyclonic gyres in promoting convection.

In section 6 we calculated the most probable distributions of heat and potential vorticity following a surface cooling event over a *composite* flow consisting of cyclonic wind forcing at the upper surface and anticyclonic flow induced by a localized seamount. Taken separately, each of these elements attracts the heat and potential vorticity introduced by convective overturning. In direct competition, however, the cyclonic gyre is shown to be the more effective process in promoting convection for the parameterized basinwide cooling event treated in this paper: even for examples in which the isopycnals are raised highest above the seamount, the cold-temperature anomaly collects in the center of the gyre (see Figs. 20 and 21).

One notable advantage of an approach based on equilibrium statistical mechanics is that we can parameterize the physical content of oceanographic phenomena and calculate the most probable end state of the fluid without resolving the detailed dynamics. In the case of open-ocean convection that is the subject of this paper, potentially this can lead to a subgrid-scale parameterization scheme for convective overturning in small oceanic basins, such as the Labrador Sea or the Weddell Sea, which are poorly resolved in global climate models. It is also relatively straightforward to incorporate other physical processes into equilibrium statistical models, such as the complications due to surface ice formation in the wintertime Weddell Sea. This may lead to a statistical theory for the onset of midwinter polynyas based on a few bulk quantities related to the circulation of the Weddell Sea and the energies in the surface ice cover and the underlying flow. (Two of the authors plan to develop this application in the future.)

In the immediate future we intend to investigate the dynamic processes that govern the distribution of heat and potential vorticity anomalies introduced by convective overturning. We plan to do this by adding well-resolved, finite-area hetons to ambient flow preconditioned by wind-driven gyres and nontrivial bottom topography and observing the temporally evolving regions of strain and coalescence of the convectively forced potential vorticity. Furthermore, by measuring the correlations between the evolving flow and the predicted most probable state for the instantaneous values of energy, circulation, and potential vorticity extrema, we can quantitatively evaluate the success of the equilibrium statistical theory in predicting the distributions of heat and potential vorticity in convectively forced damped and driven flows.

APPENDIX

Other Statistical Theories

We have based the preceding discussion on a new statistical theory (Turkington 1999) that is based on only a few conserved quantities: the energy, the vorticity extrema, and the total circulation, which is known as the Langevin statistical theory. Naturally, one may construct theories from other vortical invariants. One such model is based on only two conserved quantities, the energy and enstrophy (Kraichnan 1975), and has been successfully employed in oceanographic settings, especially in flows dominated by topography (Salmon et al. 1976; Holloway 1986; Carnevale and Frederiksen 1987)—although there are alternative interpretations—and in flows with low energies and nearly minimal enstrophy that satisfy the conditions of selective decay (Bretherton and Haidvogel 1976). In fact, the energy–enstrophy theory yields a set of mean-field equations:

$$\overline{q}_1 \equiv \Delta\overline{\psi}_1 - F(\overline{\psi}_1 - \overline{\psi}_2) = \mu_1\overline{\psi}_1 + \tilde{\gamma}_1$$
$$\overline{q}_2 \equiv \Delta\overline{\psi}_2 + F(\overline{\psi}_1 - \overline{\psi}_2) + h_B = \mu_2\overline{\psi}_2 + \tilde{\gamma}_2, \quad \text{(A.1)}$$

where μ_j are values uniquely determined by the total energy and the enstrophy in each layer that govern the fluctuations about the large-scale mean field. The additional constants, γ_j, are determined by the circulations in each layer. Notice that for the values $\mu_j = 0$ for nontrivial topography, $h_B \neq 0$, the predictions for the most probable state in the Langevin and energy–enstrophy theories exactly coincide. These are the ''zero inverse temperature'' solutions of the Langevin statistical theory: such a result is true in general for any equilibrium statistical theory (Majda and Holen 1997). This is the case for the ambient topographically induced flows described in section 3b. Also, the results given by the Langevin and energy–enstrophy theories will nearly coincide for small magnitudes of the inverse temperature.

Why, then, have we chosen to forgo the nominally simpler energy–enstrophy theory, which uses fewer conserved quantities, in favor of the Langevin theory? We have done so for two main reasons. First, the Langevin theory requires two parameters as discussed in section 2b(1) and in greater detail in DM—the potential vorticity extrema, ΔQ, and the total circulation anomaly, $\Delta\Gamma$—that occur most naturally in parameterizing the effects of convective overturning that follow surface cooling events. The essential physical content of the wind-driven ambient flows are well captured by the conserved quantities in the theory. Also, the Langevin theory is among the simplest theories that yield a *nonlinear* relation for the mean-field streamfunction that accounts for nearly all of the energy in the flow. The nonlinearity is strong at large magnitudes of the inverse temperature that defines the most probable states presented in this paper.

A second school of thought holds that equilibrium statistical theories must account for all vortical invariants conserved by ideal flow and attempt to preserve exactly the rearrangements of the initial vorticity field (Robert 1991; Miller et al. 1992). These recent theories, which are fully nonlinear, therefore require an infinite amount of information about the state of the flow. For a strongly damped and driven fluid such as the ocean the higher-order moments of the vorticity field may fluctuate rapidly in time, some lost to small scales in the enstrophy cascade, and some dissipated by viscosity. However, nearly all of these higher-order moments require more information about the instantaneous state of the ocean than is practically possible either to collect or to estimate accurately. Such theories have been used recently as a basis for parameterizing closure (Kazantsev et al. 1998).

Thus, in some sense the energy–enstrophy theory is too simple for our purposes and the infinite-constraint theories too complex. We have, therefore, elected to chart a path midway between these approaches and construct a least-biased equilibrium statistical theory for convective mixing based on just the few physical constraints that define the heton ensemble in a natural manner, as outlined in section 3.

REFERENCES

Alverson, K., and W. Owens, 1996: Topographic preconditioning of open ocean deep convection. *J. Phys. Oceanogr.*, **26,** 2196–2213.

Bretherton, F. B., and D. B. Haidvogel, 1976: Two-dimensional flow above topography. *J. Fluid Mech.,* **78,** 129–154.

Carnevale, G. F., and J. S. Frederiksen, 1987: Nonlinear stability and statistical mechanics over topography. *J. Fluid Mech.,* **175,** 157–181.

DiBattista, M. T., and A. J. Majda, 2000: An equilibrium statistical theory for large-scale features of open-ocean convection. *J. Phys. Oceanogr.*, **30,** 1325–1353.

——, and ——, 2001: Metastability of equilibrium statistical states for geophysical flows with damping and driving. *Physica D,* **151,** 271–304.

——, ——, and B. Turkington, 1998: Prototype geophysical vortex structures via large-scale statistical theory. *Geophys. Astrophys. Fluid Dyn.,* **89,** 235–283.

Grote, M. J., and A. J. Majda, 1997: Crude closure dynamics through large scale statistical theories. *Phys. Fluids,* **9,** 3431–3442.

Hogg, N. G., 1973: The preconditioning phase of MEDOC 1969: II. Topographic effects. *Deep-Sea Res.,* **20,** 449–459.

——, and H. M. Stommel, 1985: Hetonic explosions: The breakup and spread of warm pools as explained by baroclinic point vortices. *J. Atmos. Sci.,* **42,** 1465–1476.

Holloway, G., 1986: Eddies, waves, circulation, and mixing: Statistical geofluid mechanics. *Annu. Rev. Fluid Mech.,* **18,** 91–147.

——, 1992: Representing topographic stress for large-scale ocean models. *J. Phys. Oceanogr.,* **22,** 1033–1046.

Jaynes, E. T., 1957: Information theory and statistical mechanics. *Phys. Rev.,* **106,** 620–630.

Kazantsev, E., J. Sommeria, and J. Verron, 1998: Subgrid-scale eddy parameterization by statistical mechanics in a barotropic ocean model. *J. Phys. Oceanogr.,* **28,** 1017–1042.

Kraichnan, R. H., 1975: Statistical dynamics of two-dimensional flow. *J. Fluid Mech.,* **67,** 155–175.

Lab Sea Group, 1998: The Labrador Sea Deep Convection Experiment. *Bull. Amer. Meteor. Soc.,* **79,** 2033–2058.

Legg, S., and J. Marshall, 1993: A heton model of the spreading

phase of open-ocean deep convection. *J. Phys. Oceanogr.,* **23,** 1040–1056.
——, and ——, 1998: The influence of the ambient flow on the spreading of convective water masses. *J. Mar. Res.,* **56,** 107–139.
——, H. Jones, and M. Visbeck, 1996: A heton perspective of baroclinic eddy transfer in localized ocean deep convection. *J. Phys. Oceanogr.,* **26,** 2251–2266.
Madec, G., F. Lott, P. Delecluse, and M. Crepon, 1996: Large-scale preconditioning of deep-water formation in the northwestern Mediterranean Sea. *J. Phys. Oceanogr.,* **26,** 1393–1408.
Majda, A. J., and M. Holen, 1997: Dissipation, topography, and statistical theories for large-scale coherent structure. *Commun. Pure Appl. Math.,* **50,** 1183–1234.
Marshall, J., and F. Schott, 1999: Open-ocean convection: Observations, theory and models. *Rev. Geophys.,* **37,** 1–64.
Miller, J., P. B. Weichman, and M. C. Cross, 1992: Statistical mechanics, Euler's equation, and Jupiter's Red Spot. *Phys. Rev. A,* **45,** 2328–2359.
Pedlosky, J., 1979: *Geophysical Fluid Dynamics.* Springer, 624 pp.
Robert, R., 1991: A maximum entropy principle for two-dimensional Euler equations. *J. Stat. Phys.,* **65,** 531–553.
Salmon, R., G. Holloway, and M. C. Hendershott, 1976: The equilibrium statistical mechanics of simple quasi-geostrophic models. *J. Fluid Mech.,* **75,** 691–703.
Turkington, B., 1999: Statistical equilibrium structures and coherent states in two-dimensional turbulence. *Commun. Pure Appl. Math.,* **52,** 781–809.
——, and N. Whitaker, 1996: Statistical equilibrium computations of coherent structures in turbulent shear layers. *SIAM J. Sci. Comput.,* **17,** 1414–1433.